TRAPPING ULTRACOLD ATOMS IN A SUPERLATTICE

Laboratoire Systèmes de Référence Temps-Espace
in Paris Observatory

Cyrille SOLARO

MASTER THESIS
KUNGLIGA TEKNISKA HÖGSKOLAN
School of Engineering Sciences

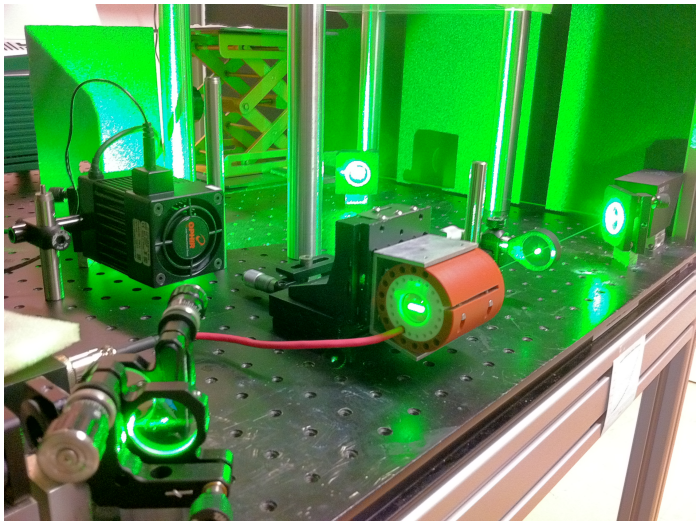

Contents

1 Introduction **1**

2 ForCa-G Experiment **3**

2.1 Principle Of The Experiment 3

2.2 Atomic Interferometry 4

2.2.1 Cooling Atoms 4

2.2.2 Ramsey Interferometer 5

2.3 Bloch Oscillations 7

2.3.1 An Optical Lattice 7

2.3.2 Manipulating Atoms In The Optical Lattice 8

2.3.3 A Superlattice 11

3 Building The Laser **13**

3.1 The DFB Laser Diode 13

3.1.1 The TEC Driver 13

3.1.2 Laser Diode's Characteristic 15

3.2 The NUFERN Amplifier 16

3.2.1 The Chiller 16

3.2.2 The Isolator 16

3.2.3 Output Of The Amplifier 17

4 Second Harmonic Generation **20**

4.1 A Short Theory 20

4.1.1 Induced Dipoles 20

4.1.2 Second Order Nonlinear Polarization 21

4.1.3 Quasi Phase-Matching 22
4.2 Our Experiment 26
4.2.1 PPSLT Crystal 26
4.2.2 Focus In The Crystal 30
4.2.3 Scheme Of The Doubling 34
4.2.4 Efficiency Of The Doubling 35

5 Building the Superlattice **38**
5.1 The Verdi 38
5.1.1 Scheme Of The Alignement 38
5.1.2 The AOM 38
5.2 My Laser 39
5.3 The Transverse Confinement 40

6 Conclusion **41**

References **43**

Chapter 1

Introduction

The project of my master thesis that I report in this manuscript has been carried out at the Laboratoire Systèmes de Référence Temps-Espace (**SYRTE**) in Paris Observatory as part of the **ForCa-G** project. The ForCa-G project, which stands for CAsimir FORce and Gravitation at short range, aims at measuring different short range interactions such as the Casimir-Polder force and at realizing a test of Newtonian gravity, searching for possible deviations to Newton gravity theory. Such deviations are made possible by new gravitational-type interactions within the range of the micrometer, as considered by various unification theories. Considering those new forces as modifications of the Newtonian gravity, one adds a so-called Yukawa potential to the Newtonian potential:

$$U_Y = U_N(1 + \alpha e^{-\frac{r}{\lambda}})$$

with $U_N = \frac{GM_1M_2}{r}$ the Newtonian potential, with r the distance between the two massive objects, α and λ being respectively the amplitude and the characteristic length of the deviation.

One can represent today's research of new interactions on a map $(\alpha - \lambda)$ (see figure 1.1 where the colored zones represent the parameter subspace excluded by the observations and measurements). At long range, interactions are pretty well described by Newtonian gravity. For example, at 1km range, the Yukawa potential is at least one thousand times weaker than the Newtonian potential. Eventual deviations to Newton gravity theory are thus negligeable when compared with Newtonian gravity. At short range though, interactions such as Van der Walls forces or Casimir forces prevail over the Newtonian potential. As a consequence it is hard to measure the Newtonian potential and thus to measure any eventual deviations from it. Thanks

to the ForCa-G experiment, we will be able to probe and exclude new zones on the $(\alpha - \lambda)$ map. The blue curve on figure 1.1 describes the predicted range of sensitivity of our experiment.

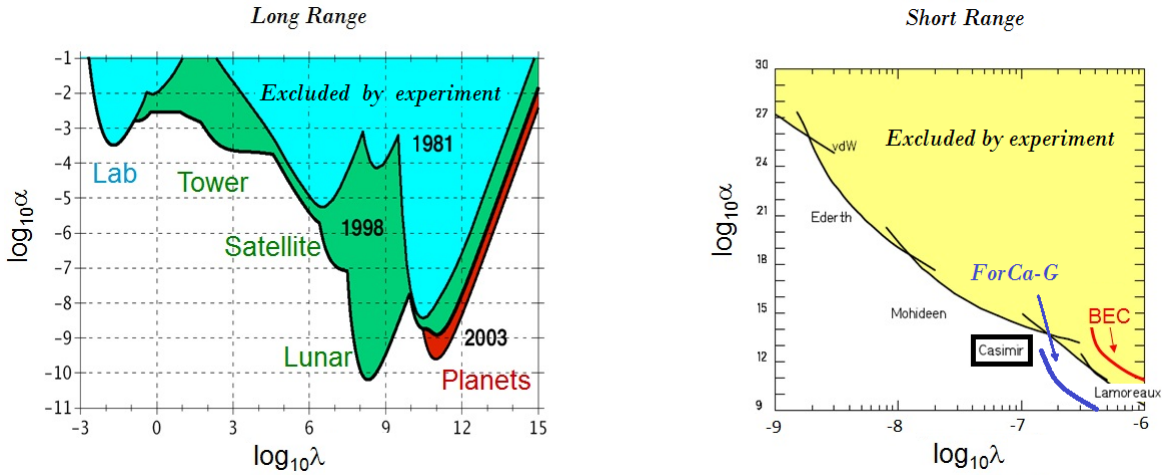

FIG. 1.1: Map $(\alpha - \lambda)$ of the deviations to Newtonian gravity at long and short ranges.

This challenging project was born in 2007 with the proposal made by P. Wolf to use trapped atoms in an optical lattice to measure short range forces [15]. Famous for its numerous experiments with cold atoms, the **SYRTE** laboratory in Paris had all the necessary know-how to host such a project. The **SYRTE** laboratory is a leader in time and frequency metrology. It has in charge several international services and is responsible for the national reference time in France. Building extremely precise atomic clocks at first, the laboratory is now developing several sensors such as gravimeters, gradiometers and gyroscopes which are also using cold atoms. Today a new generation of clocks, "optical clocks", is being investigated [14]. Such clocks, trapping cold atoms in an optical lattice to measure narrow transitions in the visible spectrum, did of course motivate the ForCa-G project as well. In the ForCa-G experiment, we trap ^{87}Rb atoms in a vertical optical lattice.

After this short introduction to the ForCa-G project and to the **SYRTE** laboratory, I will firstly explain the principle of the experiment and also the necessity of my work which consisted in building a new laser for the experiment. I will then focus on the development of this laser and I will finish with the successes and the few setbacks which stopped me from completing the project.

Chapter 2

ForCa-G Experiment

Cold atoms have proven to be a tool extremely well suited for metrology. The possibility to coherently control with high precision both the internal and external atomic states of an atomic cloud makes it a first choice technology to test the gravity (today free-fall atomic gravimeters can reach a sensitivity of $\Delta g = 2.9 \times 10^{-10} g$ as described in [10]). It is this very same tool which is used in the ForCa-G experiment. Based on atomic interferometry of trapped atoms, the experiment allows absolute measurements of the gravity with good accuracy and sensitivity ($\Delta g = 1.7 \times 10^{-7} g$).

In this section, I first present shortly the principle of the experiment and introduce to you the basics of atomic interferometry via the Ramsey interferometer. I describe next how atoms can be trapped in an optical lattice and how we can manipulate them with a Ramsey-Raman interferometer. To finish, I explain the necessity of trapping the atoms in a supperlattice if one wants to measure the Casimir-Polder force.

2.1 Principle Of The Experiment

The principle of the experiment is based on atomic interferometry. It consists in the separation of the wavefunctions of atoms trapped in a vertical optical lattice. The system is thus a superposition of wave packets localized in different wells of the optical lattice (so at different heights). After a certain time during which the phases of the wave packets evolve independently, they are recombined. One deduces from their phase difference the difference in potential energy they have been submitted to (depending on their position in the optical lattice). In a vertical

optical lattice, the difference in potential energy is nothing but the difference in the gravitational potential.

A few tenth of μm close to a surface, however, this potential is strongly dominated by the Casimir-Polder force (see figure 1.1). Realizing such a measurement close to a surface would allow us to study the Casimir-Polder force. The phase difference between atoms of different wells (ie: at different distances from the surface) would be indeed the difference in the Casimir-Polder potential experienced by the atoms (see figure 2.4). At this moment of the experiment, the atoms are trapped far away from any surface so that one measures only the gravitational potential. The current set-up that I describe briefly in this chapter allows atomic interferometry between the wells of the optical lattice and so a measurement of the gravitational potential [1][13][12][16]. The next step is to reproduce the same measurements close to a surface (the mirror used to reflect the lattice beam as described in section 2.3) in order to measure the Casimir-Polder force and eventual deviations to Newton gravity theory.

2.2 Atomic Interferometry

In 1923 Louis De Broglie suggested that matter presented the same wave-particle duality that had been verified for light since Einstein and the discovery of the photoelectric phenomenon in 1905. At that time, optical interferometry had already achieved great success with the Michelson-Morley experiment (1887), or with the Sagnac experiment (1913). When in 1927 the wave aspect of matter was verified experimentaly with the diffraction of electrons on a Ni crystal [8], atomic interferometry was predicted to meet a great success. It should for example lead to some extremely precise measurements of time (atomic clocks) or of the gravity (atomic gravimeters, gradiometers). In 1990-1991, atomic interferometry was born [5] and it met in the last two decades the foreseen success.

2.2.1 Cooling Atoms

Cooling atoms is the first step towards atomic interferometry. At low temperatures (about some μ-Kelvins) matter is more likely to show its wave aspect as well as strong quantum-mechanical properties. At room temperature an atom has a high velocity and its DeBroglie wavelength is small. When decreasing its velocity - an atom cooled down to 1μ-K has a velocity of 1cm/s - the atomic wavelength increases. It is then easier to highlight its wave characteristics and so

to perform atomic interferometry. Besides a cold atomic cloud can be easily manipulated with electric or magnetic fields and is well suited to simulate several problems of Condensed Matter Physic. For example, a system of trapped atoms in an optical lattice is similar to a system of electrons in a perfect crystal and follows the same Bloch theorem (see section 2.3). To reach such low temperatures, atoms are usually pre-cooled with magneto-optical trap (MOT) to a few μ-Kelvins and further cooled down to a few hundreds of n-Kelvins with evaporative cooling in an optical or a magnetic trap. Our team recently optained a Bose-Einstein condensate thanks to evaporative cooling in an dipolar trap. A process I won't develop in this report.

2.2.2 Ramsey Interferometer

In this subsection I give a brief overview of an atomic interferometer via the simplest example we know: the Ramsey interferometer. In a Mach-Zehnder optical interferometer, a light wave is separated in two by a beam-splitter, travels in two different "arms" and is recombined with a second beam-splitter. Similarly in a Ramsey atomic interferometer, the two different arms correspond to the two states of the hyperfine structure of the atom (here ^{87}Rb) : the ground state $|F = 1\rangle$ with an energy $\hbar\omega_g$, and the first excited state $|F = 2\rangle$ with an energy $\hbar\omega_e$. In such an interferometer, the atomic cloud is separated into the two states with a so called $\pi/2$ pulse, evolves in these two different arms and is recombined with a second $\pi/2$ pulse. Such transitions between the two hyperfine states of the ^{87}Rb atom can be easily described by the light-matter interaction. The hamiltonian of the system is the sum of the internal hamiltonian of the atom H_{at} and the coupling hamiltonian H_I:

$$\begin{aligned} H_{tot} &= H_{at} + H_I \\ &= \hbar\omega_e|e\rangle\langle e| + \hbar\omega_g|g\rangle\langle g| + \hbar\Omega_c \cos(\omega t - kz)|e\rangle\langle g| + h.c. \end{aligned} \tag{2.1}$$

with Ω_c the coupling constant of the interaction. $\Omega_c = -\frac{E_0\langle g|\hat{d}|e\rangle}{\hbar}$ with $\hat{d}$ the projection of the atomic induced dipole along the axis of the electromagnetic field $\mathbf{E}_0$. ω is the pulsation of the EM field. The wavefunction of the atom can always be written as a superposition of the ground state and the excited state:

$$|\Psi(t)\rangle = c_f(t)e^{-i\omega_g t}|g\rangle + c_e(t)e^{-i\omega_e t}|e\rangle \tag{2.2}$$

with $|c_g(t)|^2 + |c_e(t)|^2 = 1$. Inserting 2.2 into the Schrödinger equation, we get the following system:

$$\begin{cases} i\dot{c}_g(t) = \dfrac{\Omega_c^*}{2} e^{i(\delta t+\phi)} c_e(t) \\ i\dot{c}_e(t) = \dfrac{\Omega_c}{2} e^{-i(\delta t+\phi)} c_g(t) \end{cases} \tag{2.3}$$

with $\delta = \omega - (\omega_e - \omega_g)$. Solving the system assuming $\delta << \omega_{HFS} = \omega_e - \omega_g$, one obtains:

$$\begin{cases} c_g(t) = (\cos(\dfrac{\Omega_R t}{2}) - i\dfrac{\delta}{\Omega_R}\sin(\dfrac{\Omega_R t}{2}))e^{i\delta t/2} \\ c_e(t) = -i\dfrac{\Omega_c}{\Omega_R}\sin(\dfrac{\Omega_R t}{2})e^{-i\delta t/2} \end{cases} \tag{2.4}$$

with $\Omega_R = \sqrt{\delta^2 + {\Omega_c}^2}$ the Rabi frequency. The transition probability for the excited hyperfine state is thus:

$$P_e(t) = \frac{{\Omega_c}^2}{{\Omega_R}^2}\sin^2(\frac{\Omega_R t}{2}) \tag{2.5}$$

The atom oscillates between the ground state and the excited state of the hyperfine structure at the Rabi frequency Ω_R. This is called the Rabi oscillations. To separate the atoms between the two state ("arms" of the interferometer) one use a so called $\pi/2$ pulse at resonance. This "beam splitter" is defined so that $P_e = 0.5$ (half of the atoms are in the excited state and

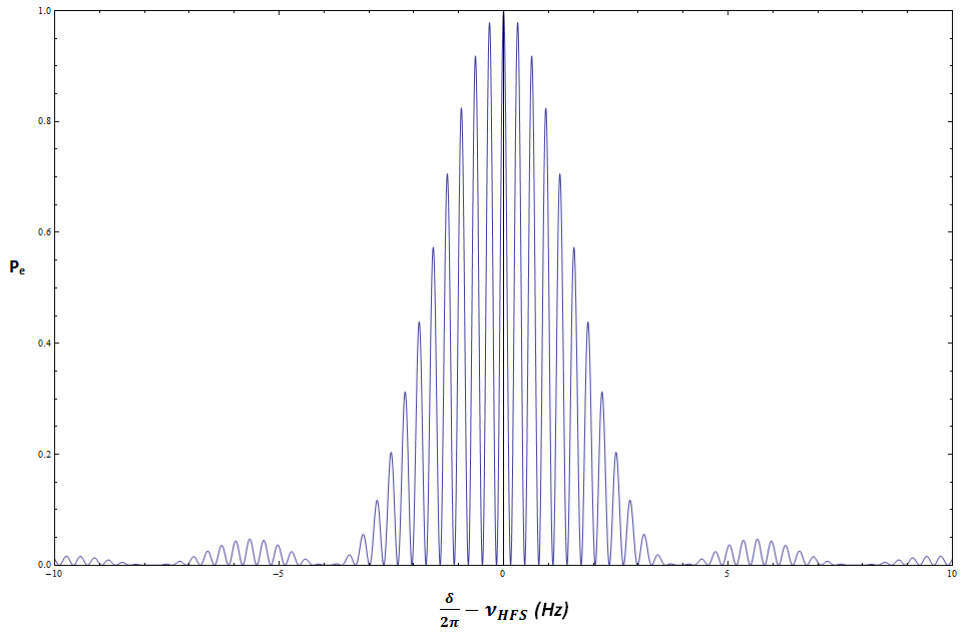

FIG. 2.1: The Ramsey interferometer, an extremeley precise way to measure the hyperfine frequency. *Calculations made with Mathematica.*

the other half remains in the fundamental state). From 2.5 one finds $\Omega_R \tau_{Ram} = \pi/2$ and $\omega = \omega_{HFS}$. Other types of beam splitter are also implemented such as Raman beams that I describe in section 2.3.2. A Ramsey interferometer is made of two $\pi/2$ pulses separated by an "interrogating" time T_{Ram}. If $\delta \neq 0$, the phase difference in the two arms of the interferometer can be written:

$$\Delta\phi = \delta \cdot t = (\omega - \omega_{HFS})t \text{ and with } t = T_{Ram} \tag{2.6}$$

$$= (\omega - \omega_{HFS})T_{Ram} \tag{2.7}$$

The wavefunction is now written:

$$|\Psi(t = \tau_{Ram} + T_{Ram} + \tau_{Ram}, \delta)\rangle = c_g(t,\delta)(1 + e^{-i\Delta\phi})|g\rangle + c_e(t,\delta)(1 + e^{-i\Delta\phi})|e\rangle \tag{2.8}$$

which leads to a transition probability:

$$P_e = |\langle e|\Psi\rangle|^2 = \frac{1}{2}(1 + C\cos(\Delta\phi)) \tag{2.9}$$

One can observe interference fringes in the frequency space with a maximum centered on the hyperfine frequency. Such an interferometer allows thus a better measurement of the hyperfine frequency. See figure 2.1. The envelope has a full width at half maximum FWHM proportional to $\frac{1}{\tau_{Ram}}$ and the interfringe is given by FWHM $\propto \frac{1}{T_{Ram}}$. The bigger the interrogating time T_{Ram}, the thiner the fringes and the better the precision on ω_{HFS}.

2.3 Bloch Oscillations

2.3.1 An Optical Lattice

In our experiment, a 532nm laser is retro-reflected on a mirror and therefore creates an optical lattice. Let us indeed consider a retro-reflected electromagnetic wave **E**. It is the sum of two contra-propagating waves with same frequency ω and opposite wavevectors $k = \pm\frac{2\pi}{\lambda}$. Assuming total reflection $R = 1$ and a phase-shift ϕ :

$$\mathbf{E} = \mathbf{E}_+ + \mathbf{E}_- = \mathbf{E}_0 e^{i(\omega t - kz)} + \mathbf{E}_0 e^{i(\omega t + kz + \phi)} \tag{2.10}$$

The boundary condition on the mirror (z=0) at t=0 leads to $\mathbf{E}_+ + \mathbf{E}_- = 0$ and $\phi = \pi$. We have now:

$$\mathbf{E} = 2i\mathbf{E}_0 \sin(kz) e^{i\omega t} \tag{2.11}$$

and the intensity I is:

$$I = \mathbf{E}_0 \cdot \mathbf{E}_0^* = I_0 \sin^2(kz) \tag{2.12}$$

which is the expression of a standing wave of period $\lambda/2$.

Atoms in such a standing wave experience a periodic potential:

$$\mathbf{F}_d = -\vec{\nabla}_{\mathbf{R}} \left(-\mathbf{d} \cdot \mathbf{E}(\mathbf{R})\right) \tag{2.13}$$

with the induced dipole momentum

$$\mathbf{d} = q_e \mathbf{r}_e = \Re\{\epsilon_0 \alpha_0 \mathbf{E}_0(\mathbf{R}) e^{i(\omega t - \phi)}\} \tag{2.14}$$

$$\Re\{\alpha_0\} = -\frac{qe^2}{2m_e \omega \epsilon_0} \frac{\delta}{\delta^2 + \frac{\Gamma}{2}^2} \tag{2.15}$$

With $\delta = \omega - \omega_{HFS}$, and ω_{HFS} the hyperfine frequency of the fundamental state of ^{87}Rb. The dipolar potential is then:

$$U_d = -\frac{\epsilon_0}{4} \Re\{\alpha_0\} E_0^2(\mathbf{R}) \tag{2.16}$$

$E^2(\mathbf{R}) = I(\mathbf{R})$ and with 2.12, the dipolar potential is indeed periodic of period $\lambda/2$:

$$U_d = -\epsilon_0 \Re\{\alpha_0\} E_0^2 \frac{1 - \cos(2kz)}{2} \tag{2.17}$$

Depending on the sign of δ, the atoms are trapped in the maxima or minima of intensity. If $\delta = \omega - \omega_{HFS} < 0$ ($\delta > 0$) the lattice is said to be blue-detuned (red-detuned) and the atoms are trapped in the minima (maxima) of intensity. In our case the laser is blue-detuned (532nm<780nm) and the wells of the potential correspond to the minima of intensity. The eigenstates of such a periodic potential follow the Bloch theorem which I won't detail here [2]. They have the same periodicity than the potential and are delocalized on all the wells of the optical lattice. They are called the Bloch states. As I explain in the next section, however, Bloch theory doesn't describe exactly our situation.

2.3.2 Manipulating Atoms In The Optical Lattice

In the ForCa-G experiment, the optical lattice is vertical so that atoms trapped in the lattice don't see the same potential depending on their vertical position. The gravity breaks the symmetry I described previously, and the eigenstates of the system are localized states. The atoms

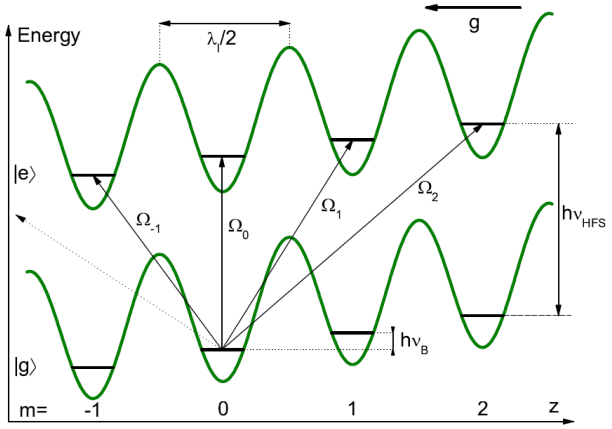

FIG. 2.2: The Wannier-Stark ladders for the fundamental state F=1 and for the hyperfine state F=2. From [1]

are thus localized on a finite number of wells which makes it possible to manipulate them and transport them from one well to another. Without going into the details of the theory, the wells of the optical lattice are shifted by an energy:

$$e = m \cdot m_{Rb} g \frac{\lambda_{latt}}{2} = m \cdot h\nu_B \tag{2.18}$$

with ν_B the Bloch frequency, m the number of the well of interest. Figure 2.2 shows the increment in energy induced by the gravity: it is a so-called Wannier-Stark ladder.

Measuring the local acceleration of gravity g at different distances from the retro-reflecting mirror requires to be able to transport the atoms in the optical lattice from one well to an

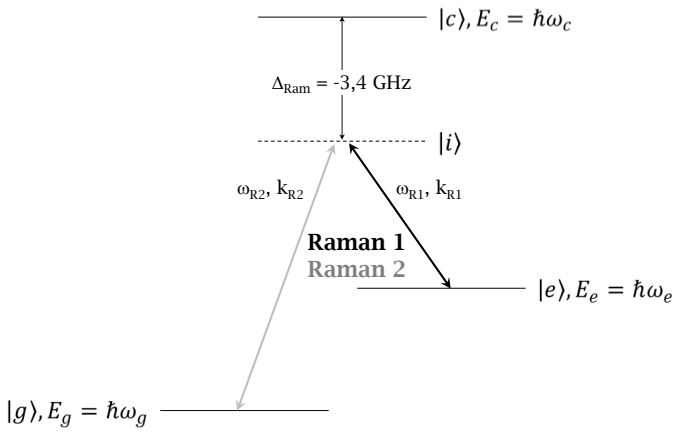

FIG. 2.3: Principle of stimulated Raman transition for ^{87}Rb. From [11]

other. To do so, we use the same ligth-matter interaction described in section 2.2.2. However one must not only change the hyperfine state of the atoms but one must also transfer to the atoms an additionnal energy so that they can jump from one well to another via tunnel effect. Stimulated Raman transitions can induce such a change both in the internal and external states of the atoms (see figure 2.3).

One use two counter-propagating Raman beams of frequency $\omega_{1,2}$ and wavevector $k_{1,2}$ so that $\omega_1 - \omega_2 = \omega_0 + m \cdot \omega_B$ and that $k_1 + k_2 = k_{eff} \approx k_{latt}$ the lattice wavevector. In a Ramsey-Raman interferometer (see figure 2.4) a first $\pi/2$ Raman pulse of duration $\tau_{Ram} = \frac{\pi}{2\Omega_R}$ transport half of the atoms in the state $|e, m\rangle$ while the other half remains in the state $|g, m = 0\rangle$. The phases of the two atomic clouds evolve independantly in the two different lattice wells during T_{Ram}. The atoms are then recombined with a second $\pi/2$ Raman pulse and one can measure with extreme precision the Bloch frequency ν_B and so the gravity g since equation 2.18. The interfringe being $\propto \frac{1}{T_{Ram}}$ the bigger T_{Ram}, the better the precision on ν_B and so on g.

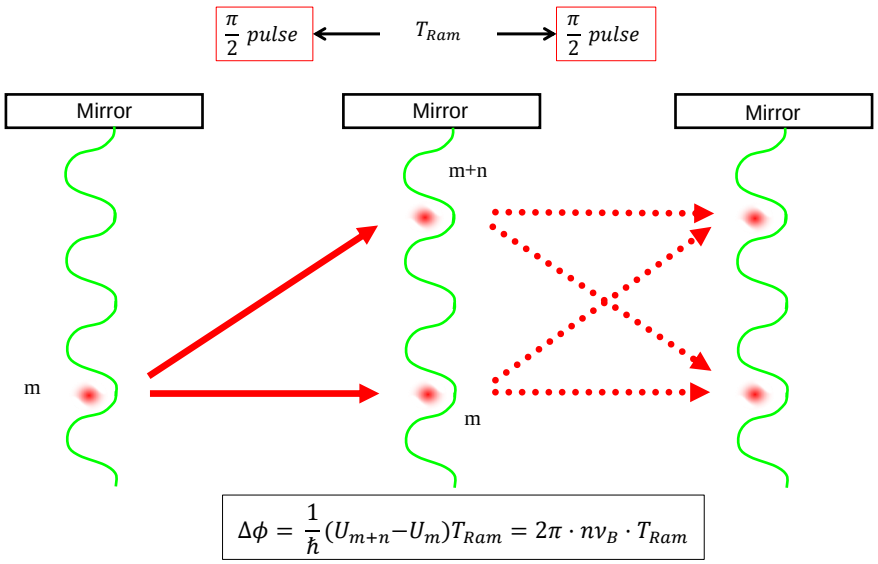

FIG. 2.4: The Ramsey-Raman interferometer in an optical lattice. The phase difference depends on the bloch frequency ν_B.

2.3.3 A Superlattice

As seen previously, each well has the same depth and the atoms are populating several wells (because of the atomic cloud size ≈ 1.5mm diameter). During a Ramsey-Raman interferometer, all the atoms in all the wells are transported at the same time of the same number of wells. Close to the retro-reflecting mirror, the phase evolution of the atoms during the interferometer is perturbated differently by the Casimir-Polder potential, depending on the distance between the atoms and the mirror. Such phase differences will induce a contrast decay of the interferometer or at best an average of the force among the different wells, leading to a less precise measurement. A modulation of this periodic potential would break this symmetry and would allow us to select atoms in only one well (in the ideal case) and regain a good contrast.

The superposition of a second laser with a different wavelength creates such a modulation of the periodic potential. This is called a superlattice. Let us consider two standing waves of wavevectors $k_1 = \frac{2\pi}{\lambda_1}$ and $k_2 = \frac{2\pi}{\lambda_2}$. Since the two beams have different wavelengths, they don't interfere and we sum their intensities.

$$I = I_1 + I_2 = I_{10}\sin^2(k_1 z) + I_{20}\sin^2(k_2 z) \tag{2.19}$$

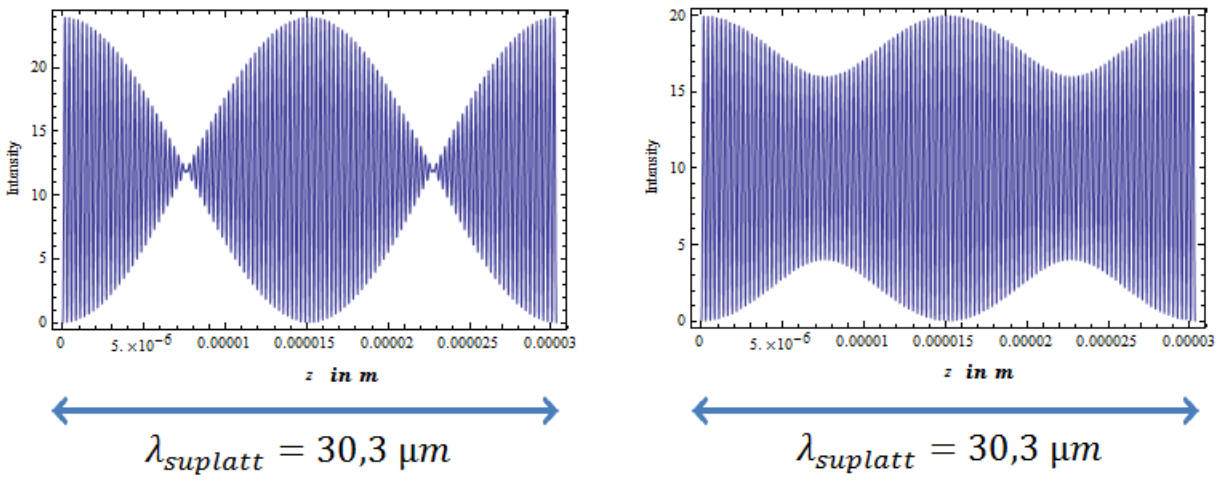

FIG. 2.5: Plots of the superlattice for different intensity ratios. On the left $I_{10}/I_{20} = 1$ and on the right $I_{10}/I_{20} = 3/4$. Note that the length of the super-periode is $\lambda_{suplatt}/2$. *Calculations made with Mathematica.*

Assuming $I_{10} = I_{20}$,

$$I = I_{10}(1 + \cos((k_1 + k_2)z)\cos((k_1 - k_2)z)) \tag{2.20}$$

In our experiment, the two lasers of the superlattice are obtained by second harmonic generation of 1064nm and 1083nm lasers. At these wavelengths, the period of the superlattice is given by (from the expression 2.20)

$$P = \lambda_{suplatt}/2 = \frac{1}{\frac{2}{\lambda 1} - \frac{2}{\lambda 2}} = 15\mu m \tag{2.21}$$

with $\lambda_1 = 532nm, \lambda_2 = 541.5nm$.

Figure 2.5 shows two plots of the superlattice for different intensity ratios. $I_{10}/I_{20} = 1$ and $I_{10}/I_{20} = 3/4$.

The first laser at 532nm is a 12W Verdi laser which is already used in the experiment to trap the atoms in a normal lattice. The second laser at 541.5nm is the one I built during this master project and which I will install on the experiment next year. High-power continuous-wave green lasers usually use frequency doubling from infrared lasers. In the next chapters I detail how I used second harmonic generation to develop such a laser.

Chapter 3

Building The Laser

The powerful current-wave green laser I built during this master project is made of three principal elements:

- A distributed feedback (DFB) laser diode as a seed laser,
- A 50W fiber amplifier
- A non-linear crystal for frequency doubling.

3.1 The DFB Laser Diode

The seed laser is a butterfly DFB laser diode from Eagleyard (EYP-DFB-1083-00030-1500-BFY02-0000). In a DFB laser, the gain medium is designed as a diffraction grating. It selects a narrow bandwidth and creates the optical feedback. This laser diode emits light at 1083nm with an extremely narrow bandwidth of 2MHz and can be finely tuned by changing the input current (0.003nm/mA) or the operating temperature (0.06nm/K). It is a very useful characteristic for phase-matching in second harmonic generation (see section 4.2.4). The laser diode has integrated Thermal Electric Cooler (TEC) and Thermistor sensor. A TEC driver remains to be built.

3.1.1 The TEC Driver

When any electric current is applied to a laser diode, it overheats quickly, causing missfunctions and strong damages to the diode. That is why every laser diode needs a TEC device to stabilize its temperature. The TEC drivers developed in the lab use the feedback of the thermistor of the diode in a control loop mechanism called PID controller (proportional-integrator-derivative

controller). PID controllers provide an easy and efficient solution for control loop feedback systems, combining at once precision, rapidity and stability. The proportional is a simple controler which increases the loop bandwidth and so the rapidity. It improves the precision and the disturbance rejection, but not the stability of the control. Indeed the higher the gain the less stable the system. Besides it has a static error. The proportional-integrator is more precise than the proportional alone. Finally, adding a derivator increases the rapidity of the system.

The transfer function of such a PID corrector is:

$$C(p) = K\frac{(1+\tau_i p)(1+\tau_D p)}{\tau_i p} \tag{3.1}$$

Where $p = j\omega$ with ω the frequency, K the gain, τ_i the integration time-constant and τ_D the derivation time-constant. These parameters have to be chosen wisely to provide a fast and stable response to a perturbation. On figure 3.1, I plotted the four possible responses to a

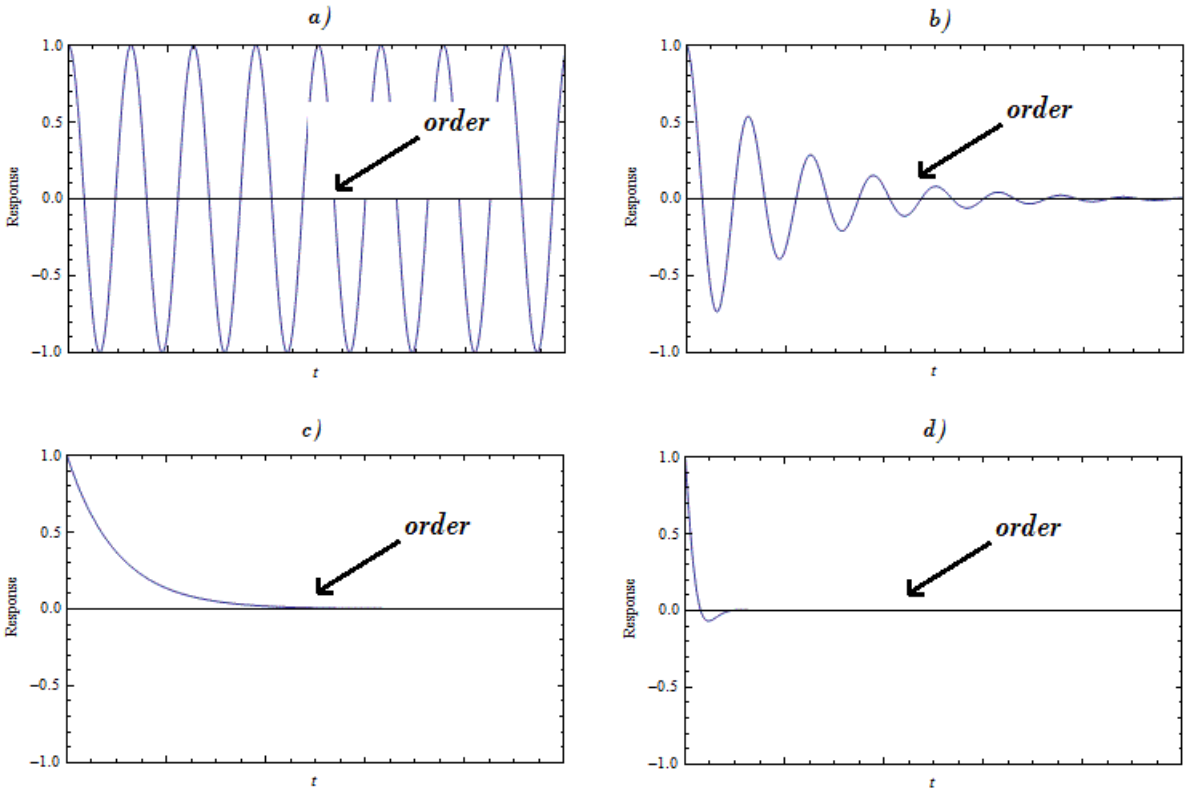

Fig. 3.1: Different responses to a perturbation at t=0. a) Oscillating Regime. b) Pseudo-Oscillating Regime. c) Attenuating Regime d) The ideal case. *Plots made with Mathematica.*

perturbation. The order is set to 0. The perturbation has an amplitude of 1. If the gain of the controller is too high, the system never stabilizes to 0. It oscillates with a free oscillatory period T_{osc}. This is the oscillating regime. If the time constants of the PID are too long, the response is too slow, the oscillations are damped, it is a pseudo-oscillating regime. Choosing the right set of resistors and capacitors so that $\tau_i = 2\tau_D = T_{osc}$ leads to an attenuating regime close to the ideal case.

3.1.2 Laser Diode's Characteristic

Once the TEC driver and the power supply were built, I could test the characteristics of the laser diode. The laser diode has a threshold at **51mA** and reaches a maximum power of **41mW** at 150mA. (see figure 3.2).

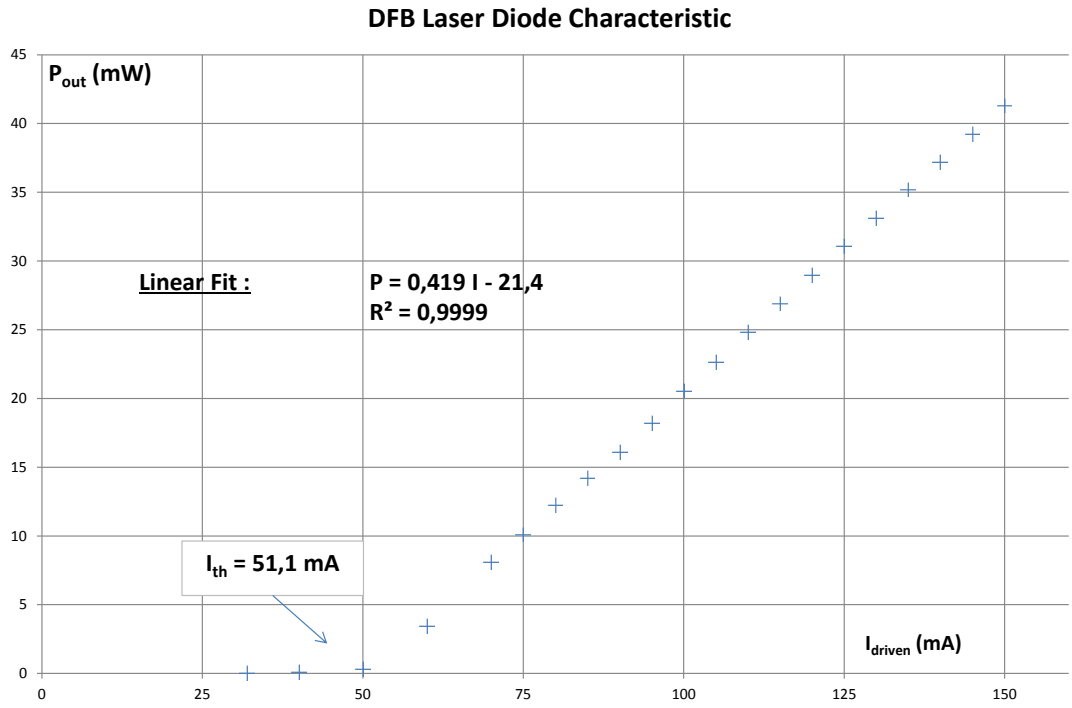

FIG. 3.2: Laser Diode's Characteristic.

3.2 The NUFERN Amplifier

Amplifying a 30mW signal into a powerful laser beam of 50W is not an easy thing at all. Fortunately, such an amplifier was already designed to that purpose and available in the laboratory. NUA-1064-PC-0050-D0 is a polarization maintaining 50W optical amplifier from NUFERN company and was designed to amplify 1064nm laser beams. It can however amplify wavelengths between 1030nm and 1100nm. I used it to amplify the 1083nm laser beam of my DFB laser diode. If the design of such an amplifier is not detailed by the manufacturer, it is probably a two level Yb-doped fiber amplifier. Before reporting the performances of the amplifier, I will shortly speak about two essential elements, the chiller and the isolator.

3.2.1 The Chiller

A chiller is a device aimed at cooling lasers or amplifiers to insure high quality performances and long life. A pump circulates a liquid through the amplifier's heat-dissipating components and the chiller removes the heat from the liquid via vapor-compression cycle. One uses distilled water to prevent any minerals from damaging the chiller. We added 5% of alcohol to prevent any bacteries from developing in the water.

3.2.2 The Isolator

An optical isolator is a device aimed at transmitting light along one direction only. It prevents possible backlight from following the reverse path and damaging optical components such as amplifiers or laser diodes. Most of optical isolators are based on the Faraday effect. In the presence of an axial magnetic field, the Faraday effect induces a rotation of the polarization of a propagating light wave. The angle of rotation depends on the wavelength and is given by:

$$\alpha = VBd$$
$$with \quad V = \frac{\alpha}{dB} = -\frac{1}{2}\frac{e}{m}\frac{\lambda}{c}\frac{dn}{d\lambda}$$

A combination of polarizing cubes and a Faraday rotator as you can see in figure 3.3 provides an intelligent optical isolator.

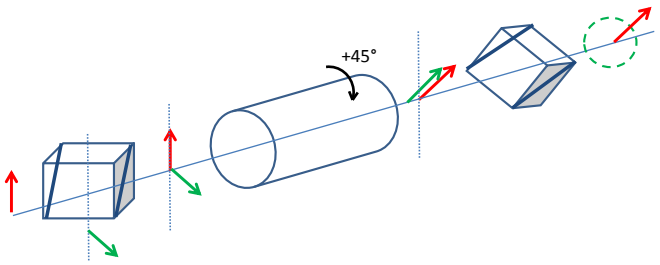

FIG. 3.3: Principle of a Faraday Optical Isolator. A suitable polarized beam can propagate from left to right (red) whereas no kind of polarized beam can propagate in the opposite direction (green).

Since the rotation angle α depends on the wavelength, by turning the second cube one can slightly change the working bandwidth of the isolator. Developped for 1064nm lasers, I experimentaly modified it so to use it with my 1083nm laser. I reached a **-31dB** attenuation in the backward direction with a forward transmission of **84%**.

3.2.3 Output Of The Amplifier

The output power

Once the chiller and the isolator were set, I turned on the amplifier and measured its performances. This mono-mode amplifier designed for a nominal wavelength of 1064nm might show different performances with my 1083nm diode laser. The figure 3.4 is a plot of the characteristic of the amplifier. For each point I waited about 5mn to estimate the fluctuations around the mean value. I wasn't disapointed by such high performances. This amplifier can reach a maximum power of **63W**. However, for some current values the fluctuations reach more than **5%** of the mean power. An interesting test was to change the seed power. I realized that it induced a short-term change in the output power of the amplifier which later stabilizes always on the same power value. Such an observation will be important to keep in mind for section 4.2.4.

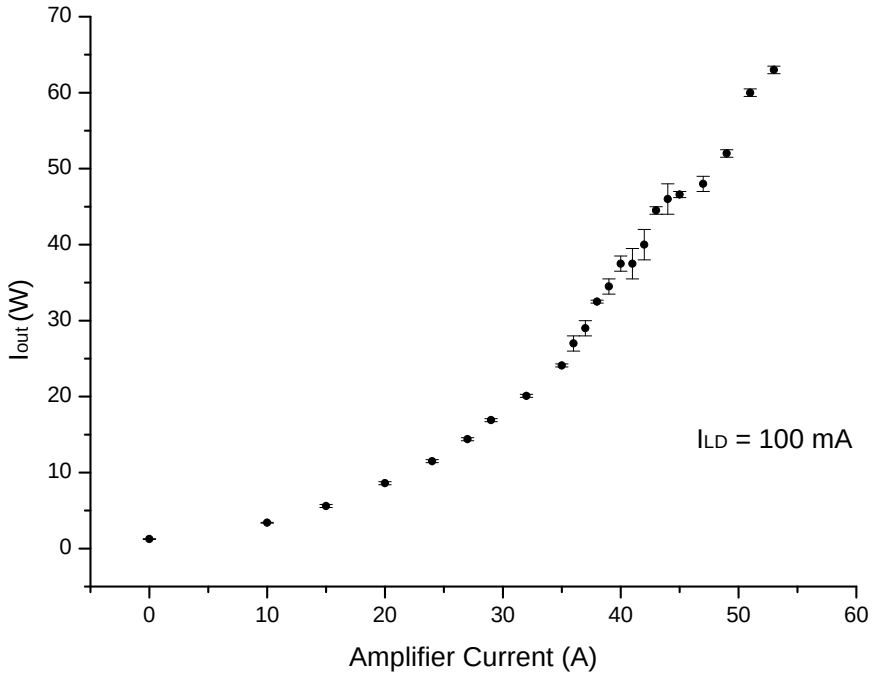

FIG. 3.4: Output power of the fiber amplifier as a function of the input electric current.

The output beam

After looking at the output power of the amplifier, I measured the quality of the output beam. Measured by the manufacturer to be of the order of $M^2 < 1.3$, I was strongly surprised by its profile. As you can see on figure 3.5, the beam isn't gaussian at all (for measurements see section 4.2.2). One can see indeed a fine-scale granular pattern : this is speckle.

When highly coherent light (such as laser light) is reflected from a surface, one can observe such a speckle pattern in the scattered spot. The same goes (to a smaller extent) for transmitted light through a lens. In fact any real surface is rough compared to the optical wavelength and scatters coherent light, creating interferences. However, in our experiment such a significant speckle can't be explained only by the roughness of the optics. By looking at the beam directly after the fiber (under no amplification) one can observe that the speckle comes from the fiber or the amplifier itself. Unfortunately, no scratches or digs could be seen on the fiber under a microscope. I tested the amplifier with a 1064nm seed laser. The output beam presented the same speckle pattern. After discussion with the manufacturer, the amplifier needed to be sent

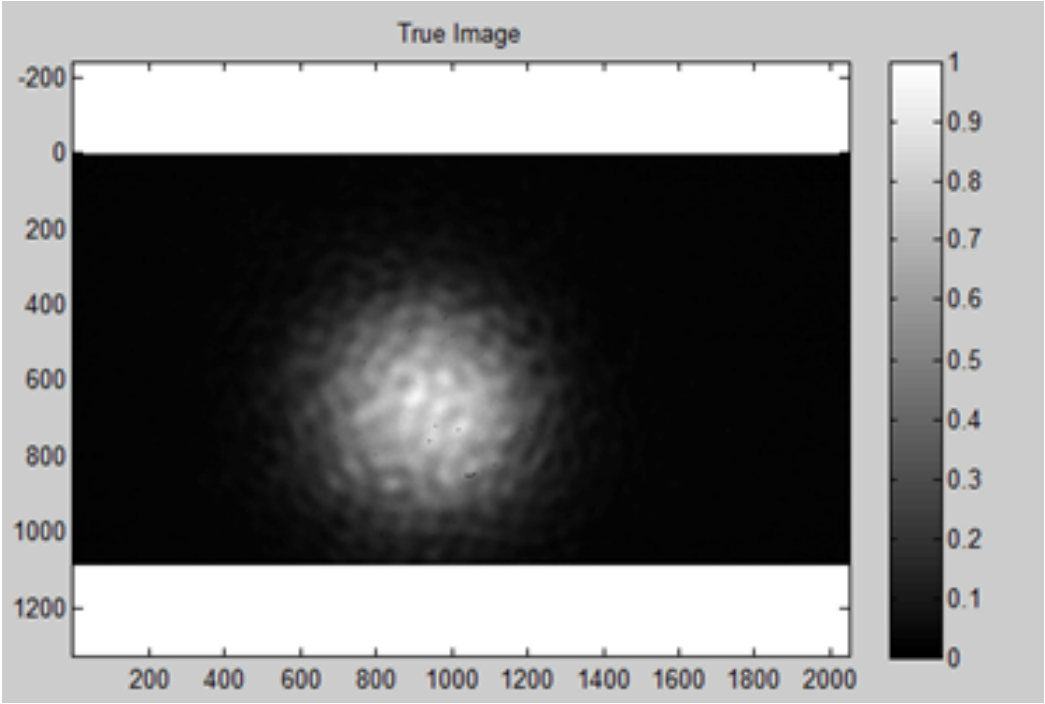

FIG. 3.5: Output beam after the fiber amplifier.

back for reparation. I postponed the reparation assuming that the quality of the beam may not affect the second harmonic generation much. Once the laser will be used to trap atoms however one will have to solve this issue. Non-uniformity of a beam due to speckle induces a random dipolar force and thus a random velocity variation of the atoms, which can strongly affects the contrast of the interferometer [7].

Chapter 4

Second Harmonic Generation

Non-linear optics plays today a key role in several applications to light sources and optical processing of information. As we have seen in section 2.3.3 second harmonic generation (SHG) is commonly used for the development of powerful lasers and is the option we chose for our experiment. In this section I present a short theory of SHG and detail how I used frequency doubling to build my laser.

4.1 A Short Theory

4.1.1 Induced Dipoles

Non-linear optic finds its origin in light-matter interaction. A static field applied on an atom acts on the electrons trajectories via the Lorentz force $\mathbf{F}$=q.$\mathbf{E}$. It induces a change in position of the center of mass of the electrons $\Delta\mathbf{x}$. As a consequence the atom behaves as a dipole $\mathbf{p}(t) = q\Delta\mathbf{x}(t)$ So when an electromagnetic field of frequency ω is applied to an atom, the induced dipole starts to vibrate due to the competition between the Lorentz force and the restoring force that links the electronic cloud to the nucleus. Lets assume an EM field propagating along the z direction and polarized along the x direction. We write it :

$$\begin{aligned}
\mathbf{E}(z,t) &= E_0 \cos(\omega t - kz)\mathbf{e}_x \\
&= (E(\omega)e^{-i(\omega t-kz)} + E^*(\omega)e^{i(\omega t-kz)})\mathbf{e}_x \\
&= (E(\omega)e^{-i(\omega t-kz)} + E(-\omega)e^{i(\omega t-kz)})\mathbf{e}_x \quad \text{since for a purely real field } E^*(\omega) = E(-\omega)
\end{aligned}$$

In linear media the induced dipole oscillates at the same frequency ω than the EM wave. Therefore the macroscopic polarization can be written:

$$\mathbf{P}(t) = Nq\Delta\mathbf{x}(t) \propto \mathbf{E} \tag{4.1}$$

with N the number of atoms (N identical dipoles).

To demonstrate this expression one must solve the equation of motion for $\Delta\mathbf{x}(t)$ (which we write x in the following). In the case of a classical harmonic oscillator :

$$\frac{d^2x}{dt^2} + \alpha\frac{dx}{dt} + \omega_0^2 x = -\frac{e}{m}\frac{\boldsymbol{x}}{|\boldsymbol{x}|}\cdot\mathbf{E} \tag{4.2}$$

with $\alpha\frac{dx}{dt}$ the damping term in a classical harmonic oscillator and $\omega_0^2 x$ the restoring force of a linear medium. The solution for a steady-state can be written :

$$x(t) = A(\omega)e^{-i(\omega t - kz)} + c.c. \tag{4.3}$$

Inserting 4.3 in 4.2, we find $A(\omega) = -e\frac{E(\omega)}{D(\omega)}$ with $D(\omega) = \omega_0^2 - \omega^2 - i\alpha\omega$ and we obtain finally :

$$\mathbf{P}(z,t) = \epsilon_0\chi^{(1)}\mathbf{E}(\omega)e^{-i(\omega t - kz)} + c.c. \tag{4.4}$$

with the linear susceptibility $\chi^{(1)} = \frac{Ne^2}{\epsilon_0 m D(\omega)}$.

4.1.2 Second Order Nonlinear Polarization

In non-linear media, the restoring force depends on the displacement of the center of mass of the electronic cloud. The equation of motion isn't linear anymore. Taking into account the second order nonlinearities, the restoring force is now written $\omega_0^2 x + \beta x^2$ with $\omega_0^2 x >> \beta x^2$. The new equation of motion is :

$$\frac{d^2x}{dt^2} + \alpha\frac{dx}{dt} + \omega_0^2 x + \beta x^2 = -\frac{e}{m}\frac{\boldsymbol{x}}{|\boldsymbol{x}|}\cdot\mathbf{E} \tag{4.5}$$

Solving this problem as a perturbated solution of the former expression, we search for a solution:

$$x(t) = \lambda_1 x^{(1)}(t) + \lambda_2 x^{(2)}(t) \tag{4.6}$$

with $\lambda_{1,2} \in [0,1]$ the strength of the perturbation. After inserting 4.6 in 4.2, since $x^{(1)}$ is solution of 4.2, the equation of motion becomes:

$$\frac{d^2x^{(2)}}{dt^2} + \alpha\frac{dx^{(2)}}{dt} + \omega_0^2 x^{(2)} = -\beta(x^{(1)^2} + x^{(2)^2}) \approx -\beta x^{(1)^2} \tag{4.7}$$

$$\begin{aligned} &= -\beta(A^2(\omega)e^{-2i(\omega t-kz)} \\ &+ 2A(\omega)A(-\omega)e^{-2i(\omega t-kz)} \\ &+ A^2(-\omega)e^{2i(\omega t-kz)}) \end{aligned} \tag{4.8}$$

Searching for a steady-state solution for $x^{(2)}$, it can be written :

$$x^{(2)}(t) = B(0) + B(2\omega)e^{-2i(\omega t-kz)} + B(-2\omega)e^{2i(\omega t-kz)} \tag{4.9}$$

Inserting 4.9 into 4.8 we derive:

$$B(0) = -\frac{2\beta e^2 E(\omega)E(-\omega)}{m^2 D(0)D(\omega)D(-\omega)} \tag{4.10}$$

$$B(\pm 2\omega) = -\frac{\beta e^2 E^2(\pm\omega)}{m^2 D(\pm 2\omega)D(\pm\omega)D(\pm\omega)} \tag{4.11}$$

We finally obtain the expression of the 2^{nd} order non-linear macroscopic polarization:

$$\begin{aligned} \mathbf{P}(z,t) &= \mathbf{P}^{(1)}(z,t) + \mathbf{P}^{(2)}(z,t) \\ &= \epsilon_0\chi^{(1)}(\omega)\mathbf{E}(\omega)e^{-i(\omega t-kz)} \\ &+ \epsilon_0\chi^{(2)}(\omega,-\omega)\mathbf{E}(\omega)\mathbf{E}(-\omega) + \epsilon_0\chi^{(2)}(\omega,\omega)\mathbf{E}(\omega)\mathbf{E}(\omega)e^{-2i(\omega t-kz)} \\ &+ c.c. \end{aligned} \tag{4.12}$$

with the linear and non-linear susceptibilities $\chi^{(1)} = \frac{Ne^2}{\epsilon_0 m D(\omega)}$ and $\chi^{(2)}(\omega_1,\omega_2) = \frac{N\beta e^2}{\epsilon_0 m^2 D(\omega_1+\omega_2)D(\omega_1)D(\omega_2)}$ with $\omega_{1,2} = \pm\omega$.

In the special case of $\omega_1 = \omega_2$, according to 4.12, the fundamental wave at frequency ω induces a vibrating dipole at frequency 2ω. This is called second harmonic generation (or frequency doubling).

4.1.3 Quasi Phase-Matching

In SHG, due to the normal dispersion in the crystal, the two waves at frequencies ω and 2ω travel at different phase velocities determined by the refractive indices $n_\omega < n_{2\omega}$. As a consequence,

the power flow oscillates between the fundamental and the second-harmonic waves and the SHG power can't grow. Lets indeed start with the non-linear wave equation in the medium.

$$\vec{\nabla} \times \vec{\nabla} \times \mathbf{E}(\omega) = \frac{\omega^2}{c^2}\mathbf{E}(\omega) + \omega^2 \mu_0 \mathbf{P}(\omega) \tag{4.13}$$

Writing for the linear case

$$\mathbf{D} = \epsilon_0 \mathbf{E} + \mathbf{P}^{(1)} = \epsilon_0(1+\chi)\mathbf{E} = \epsilon \mathbf{E} \tag{4.14}$$

assuming $\mathbf{E} = E(\omega)e^{i\mathbf{kr}}\mathbf{e}$, we obtain the Fresnel's equation:

$$\mathbf{k} \times \mathbf{k} \times \mathbf{e} + \frac{\omega^2}{c^2}\epsilon(\omega)\mathbf{e} = 0 \tag{4.15}$$

In the second order non-linear case and for frequency doubling, the Fresnel's equation becomes,

$$\mathbf{k} \times \mathbf{k} \times \mathbf{e} + \frac{4\omega^2}{c^2}\epsilon(2\omega)\mathbf{e} = 4\omega^2 \mu_0 \mathbf{P}^{(2)}(2\omega) \tag{4.16}$$

Assuming that the SHG wave is propagating along the $\mathbf{r}$ direction, $\mathbf{E} = A_{2\omega}(\mathbf{r})e^{i\mathbf{k}_{2\omega}\mathbf{r}}\mathbf{e}$, 4.16 becomes:

$$-(\mathbf{k} \times (\mathbf{k} \times \mathbf{e}) + \frac{4\omega^2}{c^2}\epsilon(2\omega)\mathbf{e})A + i(\vec{\nabla} A \times (\mathbf{k} \times \mathbf{e}) + \mathbf{k} \times (\vec{\nabla} A \times \mathbf{e})) + \vec{\nabla}(\vec{\nabla} A \times \mathbf{e}) = 4\omega^2 \mu_0 \mathbf{P}^{(2)}(2\omega)e^{-i\mathbf{k}_{2\omega}\mathbf{r}} \tag{4.17}$$

Using both 4.15 and the assumption of a slow variation of the field amplitude on a characteristic length λ, the wave equation is reduced to:

$$i(\vec{\nabla} A \times (\mathbf{k} \times \mathbf{e}) + \mathbf{k} \times (\vec{\nabla} A \times \mathbf{e})) = 4\omega^2 \mu_0 \mathbf{P}^{(2)}(2\omega)e^{-i\mathbf{k}_{2\omega}\mathbf{r}} \tag{4.18}$$

For a propagating wave along the z direction, multiplying 4.18 by $\mathbf{e}$,

$$2i\vec{\nabla} A \cdot ((\mathbf{k} \times \mathbf{e}) \times \mathbf{e}) = 4\omega^2 \mu_0 \mathbf{e}\mathbf{P}^{(2)}(2\omega)e^{-i\mathbf{k}_{2\omega}\mathbf{r}} \tag{4.19}$$

In the coordinate system ($\mathbf{D}$,$\mathbf{B}$,$\mathbf{k}$) we write (see figure 4.1)

$$-\tan(\alpha)\frac{\partial A}{\partial x} + \frac{\partial A}{\partial z} = \frac{i\omega}{n_{2\omega}c\epsilon_0 \cos^2(\alpha)}\mathbf{e}\mathbf{P}^{(2)}(2\omega)e^{-i\mathbf{k}_{2\omega}\mathbf{r}} \tag{4.20}$$

One can neglect the walk-off angle α (defined figure 4.1) and finally:

$$\frac{\partial A}{\partial z} = \frac{i\omega}{n_{2\omega}c\epsilon_0}\mathbf{e}\mathbf{P}^{(2)}(2\omega)e^{-i\mathbf{k}_{2\omega}\mathbf{r}} \tag{4.21}$$

Using the second order polarization of 4.12 into 4.21:

$$\frac{\partial A_{2\omega}}{\partial z} = \frac{i\omega}{n_{2\omega}c}A_\omega^2 \mathbf{e}\chi^{(2)}(\omega,\omega)\mathbf{e}\mathbf{e} \cdot e^{i(2\mathbf{k}_\omega - \mathbf{k}_{2\omega})z} \tag{4.22}$$

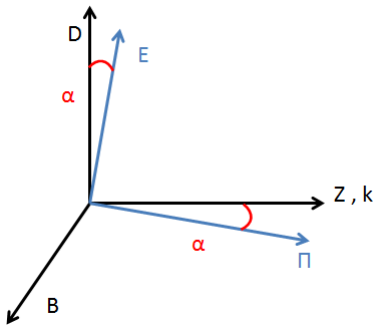

FIG. 4.1: Vectors in the coordinate system. The angle α between the wavevector k and the Poynting vector Π is called the walk-off angle.

To highlight the phase miss-matching we can write $\Delta k = 2k_\omega - k_{2\omega}$ and introduce the scalar effective susceptibility $\chi^{(2)}_{eff} = \mathbf{e}\chi^{(2)}(\omega,\omega)\mathbf{ee}$, we obtain in the end:

$$\frac{\partial A_{2\omega}}{\partial z} = \frac{i\omega}{n_{2\omega}c} A^2_\omega \chi^{(2)}_{eff} e^{i\Delta kz} \tag{4.23}$$

In the undepleted pump approximation regime ($A_\omega(z) = A_\omega(0)$), we find:

$$A_{2\omega}(z) = \frac{i\omega}{n_{2\omega}c} A^2_\omega \chi^{(2)}_{eff} sinc(\frac{\Delta kz}{2}) z e^{i\frac{\Delta kz}{2}} \tag{4.24}$$

For non phase-matched situation, equation 4.24 describes the oscillating behaviour of the intensity (see figure 4.2). The generation of the second harmonic wave occurs on a characteristic length $L_{coh} = \frac{\pi}{\Delta k}$ which is called the coherent buildup length. One can notice that the intensity of the second harmonic wave is proportionnal to the square intensity of the fundamental wave.

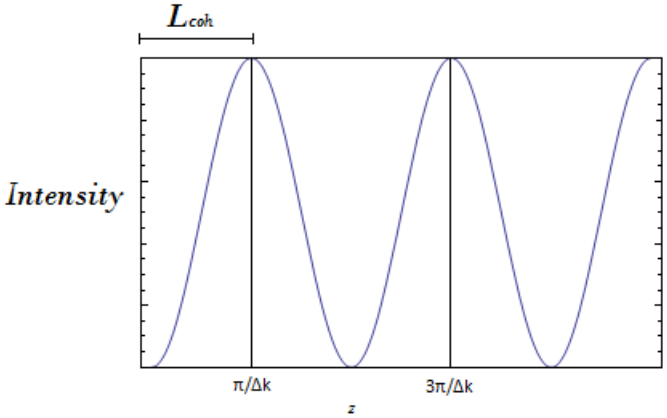

FIG. 4.2: Oscillating behaviour of the intensity of the 2nd harmonic generation in non phase-matched situation.

The most commonly used method to accomplish phase-matching is to use birefringent crystals. The refractive index of such crystals depends both on the polarization direction and the propagation direction of the EM wave. This property makes it then possible to have the fundamental wave and the SHG wave travelling at the same speed in the crystal, satisfying the phase-matching condition. Lets consider for example Type I phase-matching in a positive uniaxial birefringent crystal. In positive uniaxial crystals, the extraordinary and ordinary indices n_e and n_o verify the relation $n_e(\theta) > n_o(\theta)$ with θ the angle between the axis of the crystal and the propagation direction of the beam. We assume the fundamental wave to be extraordinary polarized and the SHG wave to be ordinary polarized. One can chose θ so that $n_e(\theta, \omega) = n_o(\theta, 2\omega)$. As a result:

$$\begin{aligned}\Delta k &= 2k_\omega - k_{2\omega} \\ &= 2\frac{n_e(\theta,\omega)\omega}{c} - \frac{n_o(\theta,2\omega)2\omega}{c} \\ &= \frac{2\omega}{c}(n_e(\theta,\omega) - n_o(\theta,2\omega)) \\ &= 0\end{aligned}$$

In isotropic materials however it is possible to realize Quasi Phase-Matching (QPM). The idea is to make the susceptibility of the crystal depending on z. For ferroelectric crystals (such as Lithium Tantalate), this can be obtained by applying electric pulses to periodic electrodes patterned on the faces of the crystal. Such "Periodically Poled" crystals provide an efficient solution to QPM (see figure 4.3). In such crystals the susceptibility is:

$$\chi^{(2)}_{eff} = \chi^{(2)}_{eff0} cos(Kz) \quad \text{with } K = \frac{2\pi}{2L_{coh}} \tag{4.25}$$

Inserting 4.25 into 4.23 we get:

$$\begin{aligned}\frac{\partial A_{2\omega}}{\partial z} &= \frac{i\omega}{n_{2\omega}c} A_\omega^2 \chi^{(2)}_{eff0} \cos(Kz) e^{i\Delta kz} \\ &= \frac{i\omega}{n_{2\omega}c} A_\omega^2 \chi^{(2)}_{eff0} \frac{e^{iKz} + e^{-iKz}}{2} e^{i\Delta kz} \\ &= \frac{i\omega}{n_{2\omega}c} A_\omega^2 \frac{\chi^{(2)}_{eff0}}{2}(1 + e^{2i\Delta kz}) \quad \text{with } K = \Delta k = \frac{2\pi}{2L_{coh}}\end{aligned} \tag{4.26}$$

Integrating 4.26 gives:

$$A_{2\omega}(z) = \frac{i\omega}{n_{2\omega}c} A_\omega^2 \frac{\chi^{(2)}_{eff}}{2} z + \text{ oscillating term} \tag{4.27}$$

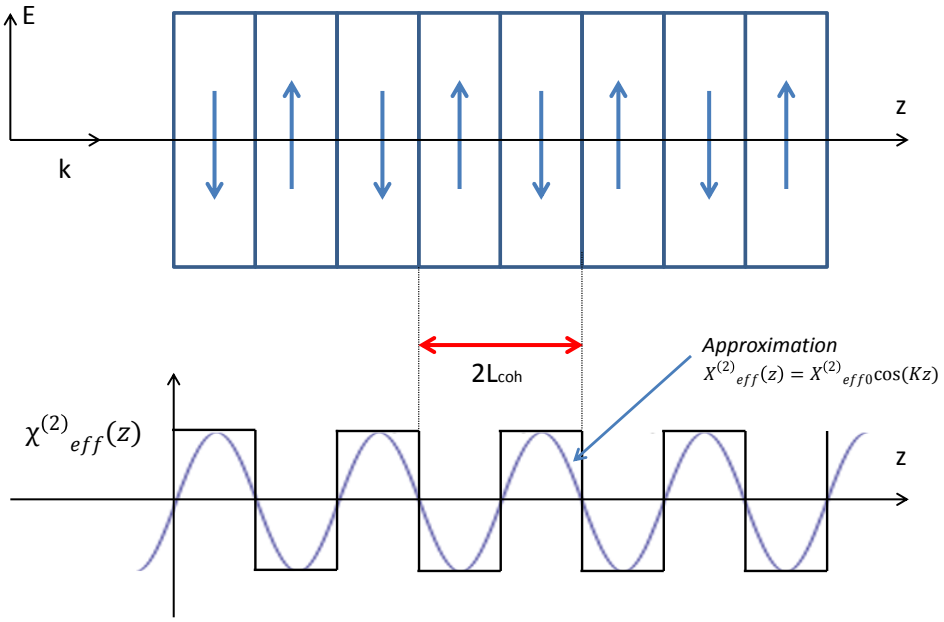

FIG. 4.3: Periodically poled crystals and effective susceptibility.

The mean amplitude increases linearly with z and quadratically with the fundamental power. Achieving QPM is interesting for many reasons. It allows phase-matching using isotropic materials or materials which are too little or too much birefringent at the wavelength of interest. One can also use nonlinear coefficients which couple waves of the same polarization. Top of all it provides a solution for SHG at any chosen wavelength and temperature.

4.2 Our Experiment

4.2.1 PPSLT Crystal

Today most commun materials for QPM SHG are Periodically Poled $KTiOPO_4$ (PPKTP) and Periodically Poled stoichiometric $LiTaO_3$ (PP:sLT). Based on the comparison made by S. Chaitanya Kumar and al. in [6], we chose to use PP:sLT in our experiment. This material provides a better temperature conductivity and thus a more stable SHG power. They also noticed a better beam quality (96% circularity) of SHG at high fundamental power 29.5W.

As we have seen in 4.1.3, the period of the PP:sLT must be chosen so that:

$$\begin{aligned} L_{coh} &= \frac{\pi}{\Delta k} \\ &= \frac{\lambda}{4(n_\omega - n_{2\omega})} \qquad (4.28) \\ &= \frac{\mathrm{P}}{2} \text{ with P the period of the grating} \qquad (4.29) \end{aligned}$$

From the Sellmeier equation for the dispersion in stoichiometric lithium tantalate [4], one can deduce the pair of parameters $\{P, T\}$ for the fundamental wavelength of interest 1083nm (see figure 4.4).

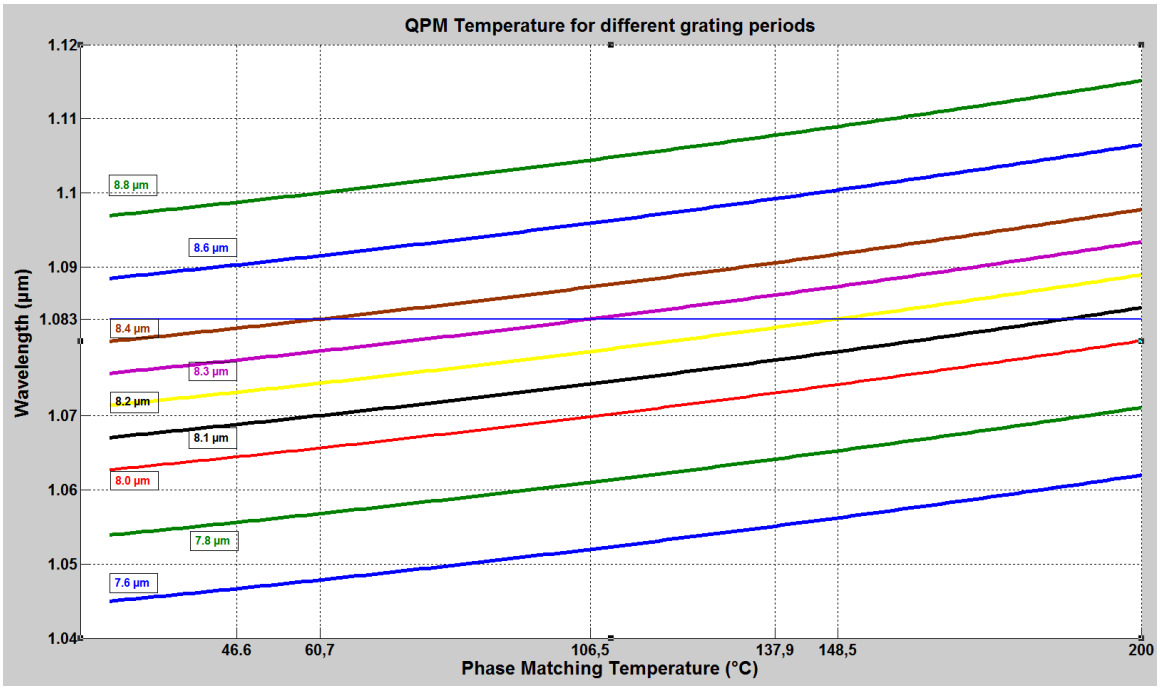

FIG. 4.4: For different grating periods, the phase-matching temperature as a function of the wavelength. *Calculations made with Matlab*

The Sellmeier equation gives results with an accuray of ±1.5nm for SHG. The graph verifies this accuracy. From this simulation, four working points are interesting for us : $\{8.4\mu m, 60.7°C\}$, $\{8.3\mu m, 106.5°C\}$, $\{8.2\mu m, 148.5°C\}$, $\{8.1\mu m, 187.2°C\}$. The manufacturer (Deltronic Crystal Industries) delivered to us a crystal with different periods $\{8.0, 8.2, 8.4, 8.6, 8.8, 9.0, 9.2\}$. Limited by the oven performances ($T < 200°C$) the only two possible pairs of parameters are

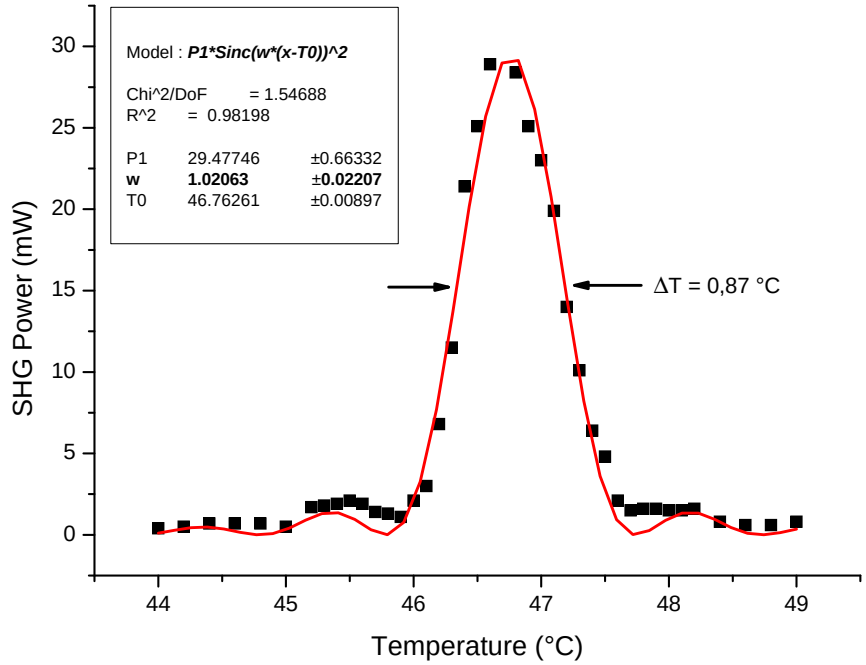

FIG. 4.5: Temperature tuning curve, for a fundamental power of 1.3W.

$\{8.2\mu m, 148.5°C\}$ and $\{8.4\mu m, 60.7°C\}$ (or $\{8.2\mu m, 135°C\}$ and $\{8.4\mu m, 50°C\}$ according to the manufacturer). So I began with the 8.4 μm period and at low fundamental power I ploted the temperature tuning curve to find the phase-matching temperature (see figure 4.5). The resolution of the oven temperature controller is $0.1°C$. A fit of the curve with a $sinc(x)^2$ function gives a phase-matching temperature of $\mathbf{46.76}°C$ and a temperature acceptance bandwidth (FWHM) of $\mathbf{0.87}°C$. A value a bit lower than the expected $0.96°C$ using the Sellmeier equation and the relation [9]:

$$\Delta T = \frac{0.4429\lambda_\omega}{L}\left[\frac{\partial n_{2\omega}}{\partial T} - \frac{\partial n_\omega}{\partial T} - \alpha(n_{2\omega} - n_\omega)\right] \tag{4.30}$$

I progressively started increasing the IR fundamental power. Due to thermal effects in the crystal introduced by the fundamental beam, the phase-matching temperature decreases (see figure 4.7). Finding back the phase-matching temperature for each fundamental power takes time since the response of the oven is long (a few minutes).

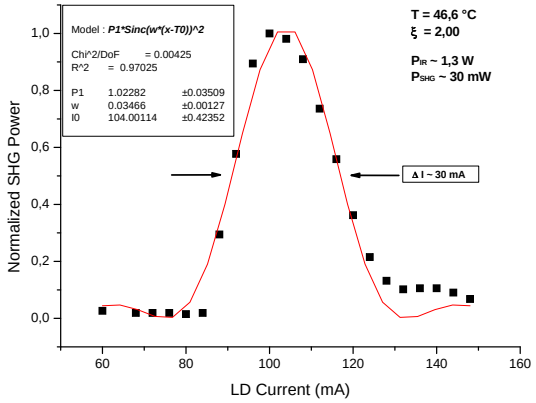

FIG. 4.6: Spectral tuning curve, for a fundamental power of 1.3W

However as we said in section 3.1, the bandwidth of the laser diode can be tunned by changing the current. Increasing the input current increases the wavelength. By knowing roughly of how much I changed the current, I can thus deduce of how much the oven's temperature needs to be shifted. One must yet be cautious to just change lightly the seed power not to affect the amplifier output power (discussed in section 3.2.3). I plotted the efficiency of the SHG with respect to the input current of the laser diode (figure 4.6). The wavelength increases linearly with the current. To a FWHM of 30mA in current corresponds a FWHM of 0.003nm$\times$ 30 = **0.09nm**. Using the acceptance spectral bandwidth relation from [9]:

$$\Delta\lambda = \frac{0.4429\lambda_\omega}{L}\left[\frac{n_{2\omega}-n_\omega}{\lambda}+\frac{\partial n_\omega}{\partial\lambda}-\frac{1}{2}\frac{\partial n_{2\omega}}{\partial\lambda}\right] \tag{4.31}$$

one obtains a FHWM acceptance bandwidth of **0.2nm**. This result is close to what I measured experimentaly. This quantifies the finesse of the spectral tuning required for optimizing the SHG.

For different fundamental powers, without optimizing anything but the temperature (and also the spectral tunning), I measured the SHG power (see figure 4.7). At about 25W of fundamental power, the temperature locking system of the oven doesn't work anymore. The laser heats the crystal too much. The oven is meant to heat up the crystal and not to cool down the crystal. As a result the quasi phase-matching condition can't be reached. I decided then to switch to the second period $\{8.2\mu m, 135°C\}$. The final results with the 8.2μm period are presented in subsection 4.2.4.

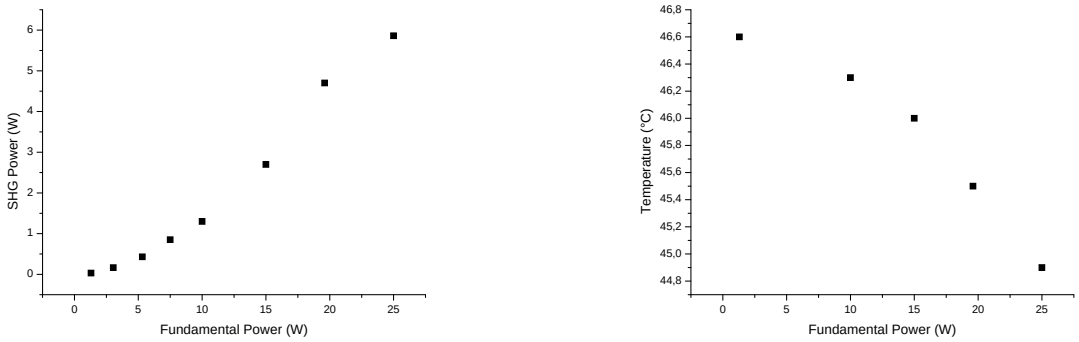

FIG. 4.7: On the left is a plot of the second harmonic generation power as a function of the fundamental power in the 8.4μm period. On the right is a plot of the evolution of the Phase-matching temperature versus the fundamental power in the 8.4μm period. At 25W the temperature phase-matching condition can't be reached.

4.2.2 Focus In The Crystal

The focusing parameter

A very important geometric parameter for SHG is the focusing parameter ξ. This parameter defined as

$$\xi = \frac{L}{b} \tag{4.32}$$

quantifies the ratio of the length of the crystal L over the Rayleigh length of the fundamental beam in the crystal $z_r = b/2$. Let's recall for a gaussian beam that the Rayleigh length is directly related to the waist of the beam by

$$\begin{aligned} z_r &= \frac{\pi {w_0}^2}{\lambda} \\ &= \frac{\pi {w_0}^2 n}{\lambda_0} \end{aligned}$$

with n the refractive index of the crystal, λ_0 the fundamental wavelength in vacuum and w_0 the waist of the fundamental beam. According to the work of Boyd and Kleinman [3], in our situation (for a double refraction parameter B=0), the optimal focusing parameter is $\xi = 2.84$ (see figure 4.8)

Applied to our situation with L=40mm,

$$\begin{aligned} w_0 &= \sqrt{\frac{L\lambda}{2\xi\pi n}} \\ &= 33.7\mu m \end{aligned} \tag{4.33}$$

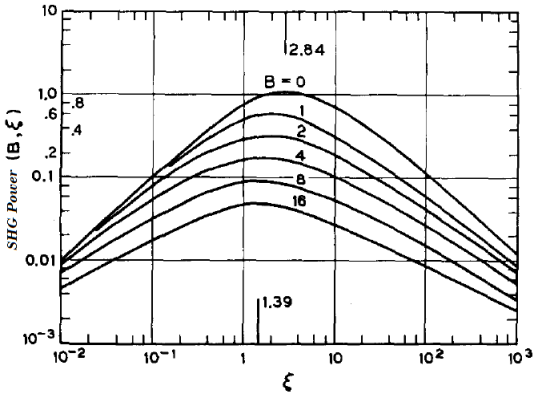

FIG. 4.8: SHG power as a function of the focusing parameter ξ and the double refraction angle parameter B. Calculations and figure from [3]

Characterizing ξ

A small set of lenses can be used to obtain such a waist. I spent a long part of my project characterizing this focusing parameter for different focusing lenses and fundamental powers. To measure the beam waist at different positions after the focusing lens, I used a CCD camera (BeamAge-0.3 from Gentec). As the camera software didn't work properly, I had to write a Matlab script to process the images. The matlab script I developed measures the waist of a gaussian beam both along the vertical and horizontal directions. Since the common bitmap files recorded by the CCD software are of no use to quantify the beam intensity, I had to work with .txt files. The script creates a 2D matrix of the size of the image. It sums all the lines (respectively the columns) to average possible speckle. It fits then the gaussian beam with the matlab function *lsqcurvefit* which solves problems in the least-squares sense, and determines the beam waist along the vertical (respectively the horizontal) direction (see figure 4.9).

Characterizing ξ in my experiment was not without any complications. Indeed the speckle I presented in section 3.2.3 strongly affects the quality of the beam profile. The beam isn't gaussian and doesn't follow the gaussian laws for beams propagation. The figure 4.10 presents this work. In gaussian optics, the evolution of the waist of a gaussian beam in free space is given by:

$$w(z) = w_0\sqrt{1+\frac{\lambda z}{\pi\omega_0^2}^2}$$
$$= w_0\sqrt{1+\frac{z}{z_r}^2}$$

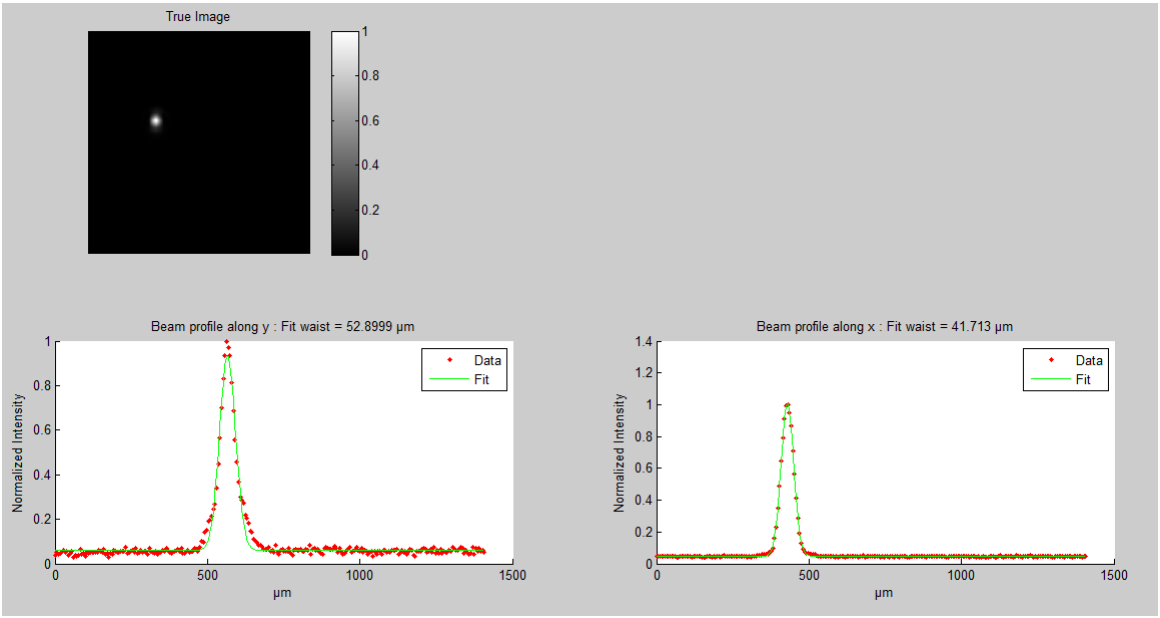

FIG. 4.9: Example of my script window

with $z_r = \frac{\pi\omega_0^2}{\lambda}$ the Rayleigh range.

From this kind of plots one could estimate the quality of the beam profile. A real beam doesn't follow the gaussian laws of propagation. The Rayleigh range is reduced by a factor M^2 (the beam quality factor). Unfortunately I made these measurements between the Rayleigh range so that one can not deduce M^2 by fitting these curves. It is however interesting to notice that if at low power (1.3W) the beam profiles look gaussian and circular ($\omega_x \approx \omega_y$), strong astigmatism (between 2 and 6 mm) appears at high power (30W). Top of all, when the power increases the medial focus is translated backwards. This can be explained by thermal effects in the lenses, either in the output collimator or in the focusing lense (see the scheme of the doubling 4.11). An intelligent set up of cubes and half-wave plates placed before the focusing lenses could answer that question. This phenomenom needs anyway to be taken into account while optimizing the alignement of the crystal for SHG (see figure 4.13).

One can deduce the focusing parameter ξ from such waist measurements. However since the beam is not gaussian, a proper characterisation of ξ would have required a measurement of the divergence of the beam at long range (not within the Rayleigh range as I did). Although to get an idea of ξ, I decided to calculate the focusing parameter with equation 4.33 and the measured waist value (see table 4.1). I chose to use the 200mm focal lense which induce a

Focal Length (mm)	Power	Waist (μm)	ξ
150	1.3 W	27.3	4.34
150	30 W	29.7	3.66
200	1.3 W	40.2	2.00
200	30 W	43.8	1.68
250	1.3 W	47.9	1.41
250	30 W	52.15	1.19

TAB. 4.1: Table representing the focusing parameter for different configurations.

focusing parameter close to the optimum. The beam is less focused than it should be to have the best efficiency but it will reduce thermal effects in the crystal.

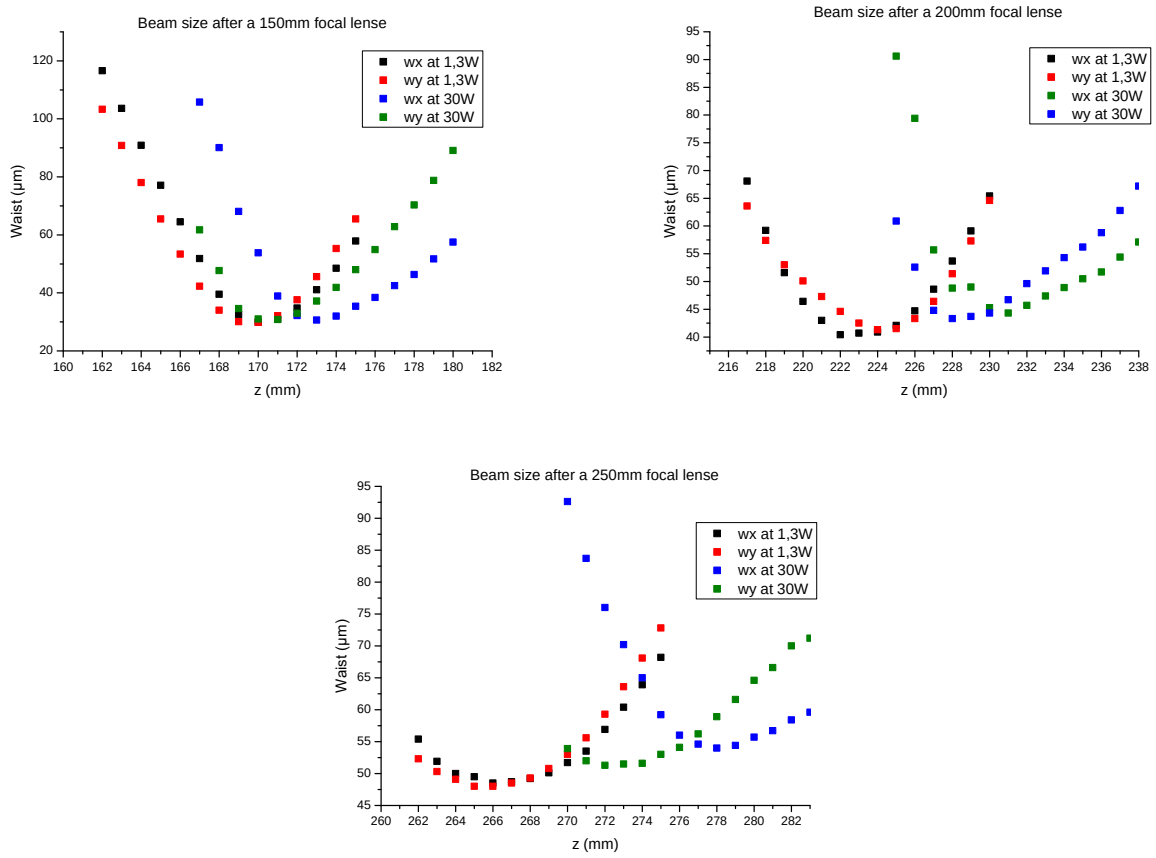

FIG. 4.10: Thermal effects. Different waists measurements at different power. Top Left : after a lense of focal length f=150mm. Top Right: after a lense of focal length f=200mm. Bottom : after a lense of focal length f=250mm.

4.2.3 Scheme Of The Doubling

Figure 4.11 shows the set up of the experiment. The first half-wave plate corrects the polarization to inject the beam in the optical isolator with a maximum of transmission (see 3.3). Both the collimator and the optical isolator are at 60mm high whereas all the optics in ForCa-G experiment are at 40mm high. The two mirrors placed after the isolator form a periscope to work at 40mm high. The second half-wave plate sets the required polarization for SHG in the crystal. The lens *L1* focuses the beam into the crystal $\{f' = 200, 150, 100\}$. The crystal 1.0mmx8.2mmx40mm is placed in a specific oven of length 40mm+20mm and diameter 50.8mm. The mounting system I developed with the workshop team of SYRTE allows two directions of translation for the crystal (figure 4.12). One along the axis of the crystal to follow the displacement of the waist when I increase the power (see previous section). And the second along the transverse direction to choose between the periods of the multi-grating QPM crystal.

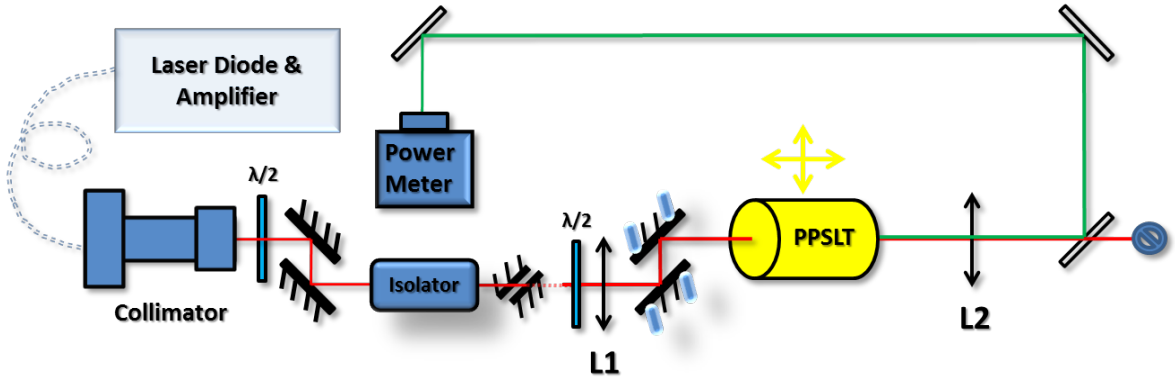

FIG. 4.11: Scheme of the SHG experiment.

To align the beam along the third direction (the vertical) and once again along the horizontal, I use two mirrors with an extremely fine adjustement (Four D22 from Thorlabs with a pitch : 0.5μm per graduation). Thanks to those four differential manual adjusters I can optimize the SHG efficiency at high power whithout being likely to shoot outside the crystal. The lens *L2* collimates the beam. It is a double-V-coated lens made for high power lasers working at 1064/532nm such as YAG lasers. Finally three dichroic mirrors are placed on the beam trajectory to get rid of the residual IR light.

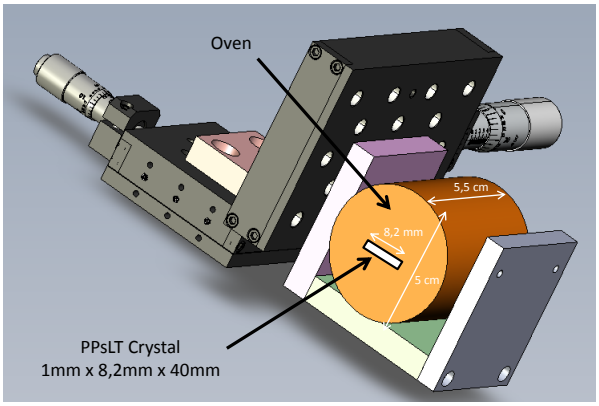

FIG. 4.12: Mounting system developped at SYRTE with the workshop team.

4.2.4 Efficiency Of The Doubling

Thanks to this set up, I could reach good results within the state of the art for single-path frequency-doubling in non-linear crystals. I used the 200mm focal lense which corresponds to $\xi \approx 2.0$. The two next graphs (4.13) show how thermal effects in the crystal or in the lenses affects the SHG and how I compensate it. The phase-matching temperature drops by $\mathbf{2}°C$ between 1.3W and 30W of fundamental power. I translated the crystal of **15mm** to

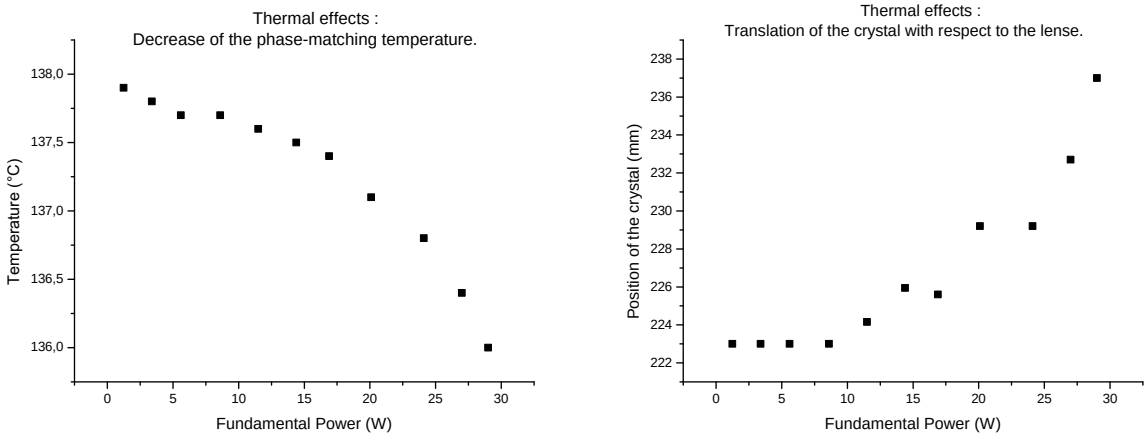

FIG. 4.13: The compensation of thermal effects. On the left is a plot of the decrease in the phase-matching temperature. On the right is a plot of the displacement of the crystal along the longitudinal direction

compensate the displacement of the fundamental beam waist. This value is twice as much as the waist displacement expected from graph 4.10. This can be explained by the fact that the optical path in the crystal is multiplied by the refractive index $n \approx 2$.

The SHG conversion follows well the expected quadratic dependence calculated in 4.27 for low powers up to $\approx 17W$ of IR power (see figure 4.14). For higher fundamental powers, the variation seems to be linear. Equation 4.27 doesn't describe the conversion anymore. One can certainly not use the undepleted pump approximation anymore. I could reach a SHG power of **10W** with an efficiency of **34.2%**. (see figure 4.15). These curves let us imagine that I may not have reached the maximum SHG power the crystal can provide yet.

Unfortunately the crystal broke during an mechanical optimization of the SHG power. Due to the waist displacements in the crystal, I had to optimize the alignment at high power for each different fundamental power, a tricky operation. By translating the crystal too fast, I may have created a temperature gradient, producing a thermal shock into the crystal. Another explanation would be that a dust may have sticked to the crystal, heating it inhomogeneously and producing a thermal shock as well. To prevent this from happening again, I will design a plexiglas box around the oven to protect the crystal. This missfortune stoped me from completing my work. Besides trapping the atoms in the supperlattice, it would have been interesting to test the SHG with different set of lenses and to verify the work of Boyd and Kleinman on the focusing parameter ξ.

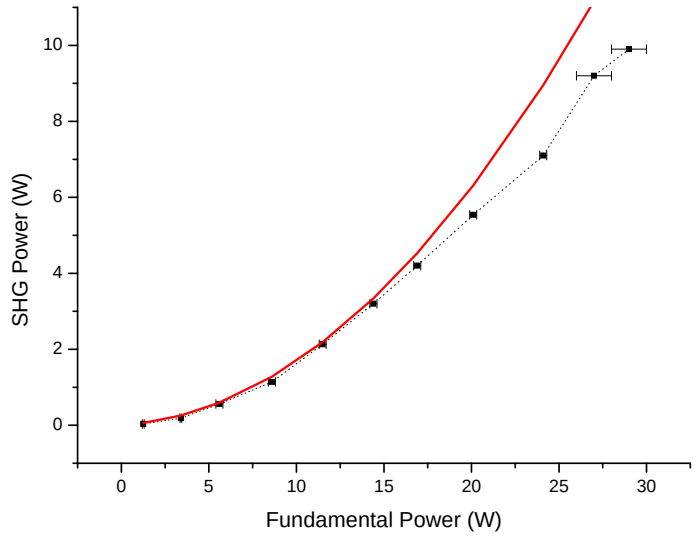

FIG. 4.14: The second harmonic generation power as a function of the fundamental power.

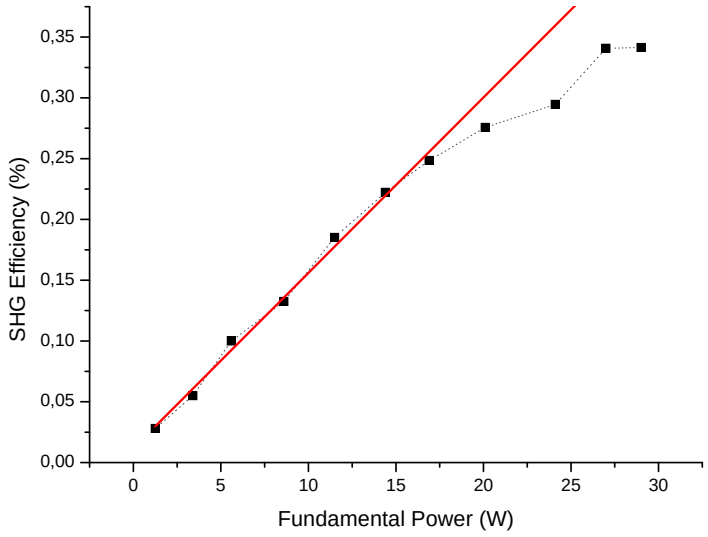

FIG. 4.15: The efficiency of the second harmonic generation as a function of the fundamental power.

Chapter 5

Building the Superlattice

5.1 The Verdi

Already used in the first ForCa-G experiment, the Verdi laser is a 532nm laser created via second harmonic generation of a Nd:YAG laser. It was developed by Coherent company.

5.1.1 Scheme Of The Alignement

As we have seen already in the subsection 2.3, the standing wave is created via a retro-reflective mirror placed on the top of the vacuum chamber. Making sure that the standing wave is perfectly vertical is not an easy thing to do. To do so, we firstly placed a liquid mirror (a glass filled with water) on the top of the vacuum chamber to reflect the incident beam. The reflection of interest is the one which doesn't move when one tilts the glass. Playing with the mirrors, we could make the reflected beam and the incident beam overlap. The optical lattice is then perfectly vertical. Let us precise that working with a green laser had two practical advantages. Since the human eye is fully sensitive to green light, we didn't need infrared viewer and a few mW of power was sufficient to realize such an alignment. The scheme of the Verdi alignment is presented on figure 5.1 It is the light green part at the bottom of the scheme.

5.1.2 The AOM

An acousto-optic modulator (AOM) uses the acousto-optic effect to diffract a light wave. When a sound wave is transmitted through the crystal of an AOM, its refractive index changes periodically due to the pressure fluctuations into the crystal. This generates a diffraction gratting

an leads to Bragg diffraction. At the output of the AOM, one can see the different orders of diffraction which angles θ_m are given by : $sin(\theta_m) = \frac{m\lambda}{\Lambda}$ where Λ and λ are respectively the wavelengths of the sound wave and the light wave, and m = -2,-1,0,1,2,... the order of diffraction. One can control the amplitude and the frequency with a RF signal. In our experiment, we use AOMs to be able to switch on/off the lasers. The zeroth order is sent to a beam dump while the first order is directed towards the atoms.

5.2 My Laser

If the breakage of my crystal stopped me from installing my laser on the ForCa-G experiment, I designed the set up I would have implemented and I added a scheme of it on the existing scheme of the ForCa-G experiment (see figure 5.1). My laser with its optical path is represented in the light blue part on the top right angle of the figure. The two lasers can be switched on or off separately with two different AOMs. They are combined with a polarizing cube.

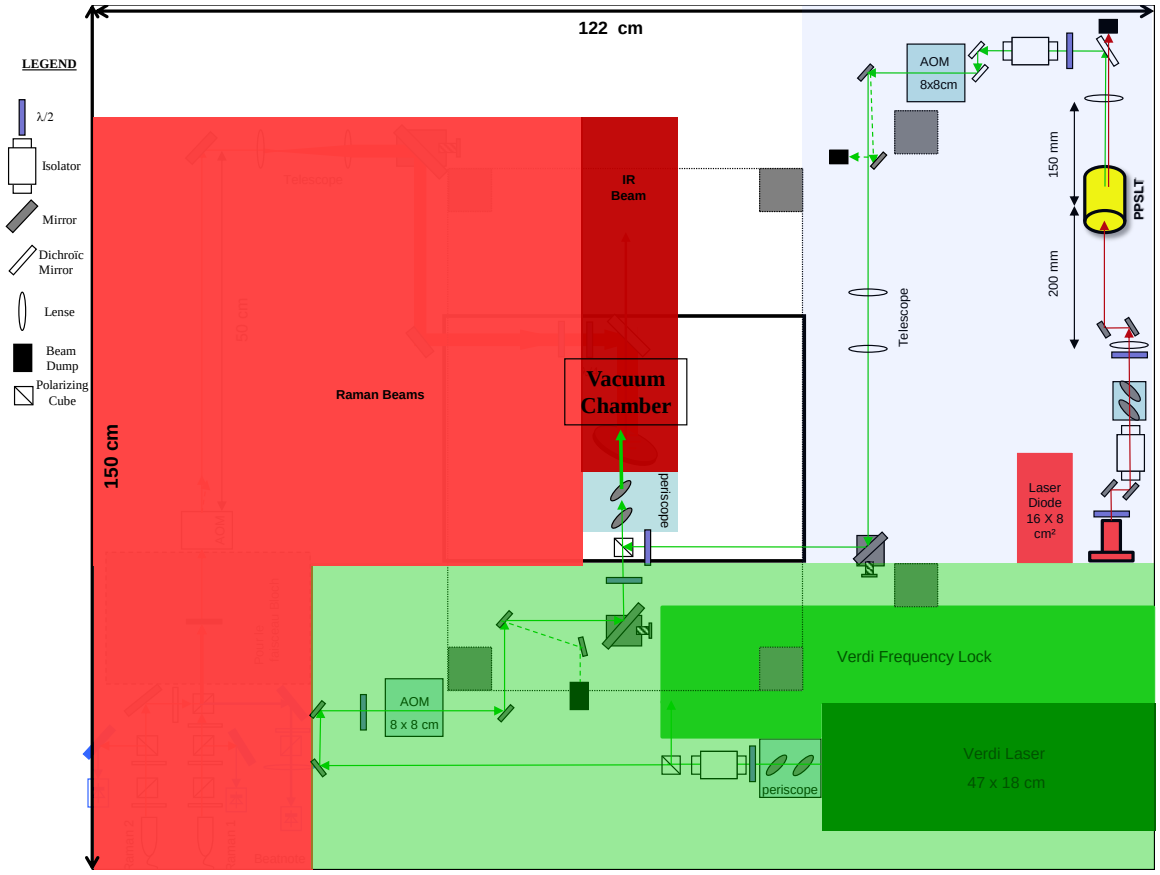

FIG. 5.1: My laser on the ForCa-G experiment table.

5.3 The Transverse Confinement

We should notice that our superlattice is only one dimensional. As a result nothing prevents the atoms from distributing along the horizontal plane and thus from escaping the superlattice. In order to keep our atoms in the superlattice, we use a red-detuned laser beam at 1064nm focused on the atoms cloud position. This is the transverse confinement beam as you can see on figure 5.2.

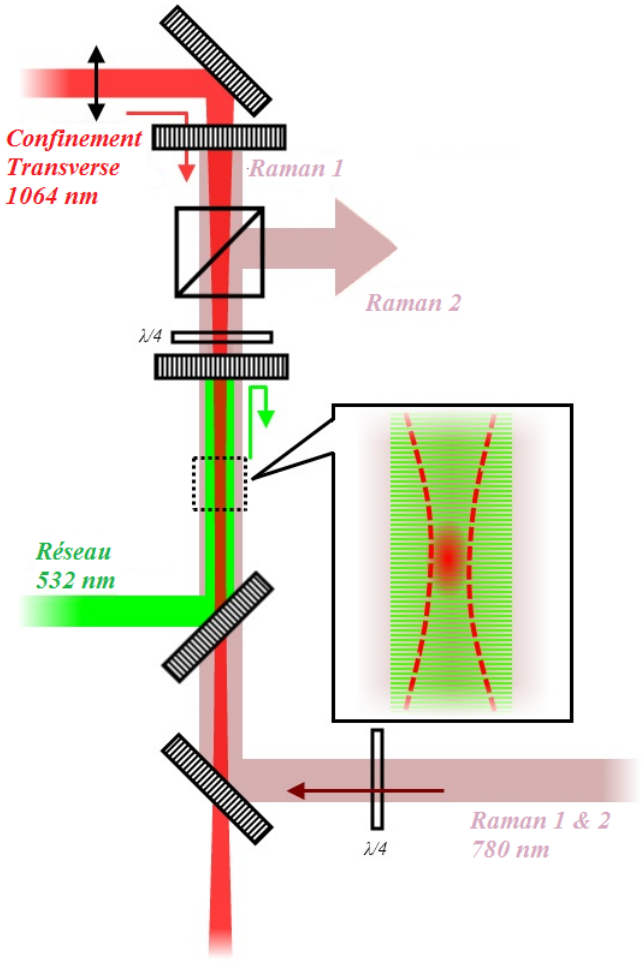

FIG. 5.2: The ForCa-G optical set-up. The atoms are trapped in the green lattice and confined transversally with the IR beam. The two Raman beams perform atomic interferometry. From [11]

Chapter 6

Conclusion

I presented in this manuscript both the design and the realization of a 10W continuous-wave green laser. This master project which has been carried out at the Laboratoire Systèmes de Référence Temps-Espace (**SYRTE**) in Paris Observatory was part of the **ForCa-G** project. Indeed essential to the ForCa-G experiment, the aim of my laser is to trap atoms in an optical supperlattice in order to study short range forces such as the Casimir-Polder force. After presenting briefly the principle of the ForCa-G experiment and the necessity to build such a laser, I focused on the three different parts of development of this laser: the seed laser, the amplifier and the second harmonic generation in a PPs:LT crystal. Unfortunately the breakage of the non-linear PPs:LT crystal stopped me from building the supperlattice and trapping the atoms. I demonstrated however that my laser fulfilled the requirements of the ForCa-G experiment.

During this master thesis, I learned a lot both about laser physics and atomic physics. I was confronted to several experimental problems and I worked out different solutions. Optimizing all the different parameters I discussed in this manuscript was not easy. However I learned that the more parameters you can change the best chances you get to perform a good experiment.

Acknowledgments

I want to thank all the people who helped me during my master project and whithout whom I would not have successfully achieved this work. Working with the ForCa-G team is a pleasure and I am glad to be part of it.

First I want to thank Franck, my supervisor, for adopting me in his team during my master project. Thank you for all your numerous explanations and your help concerning the different administration issues. Thank you for pushing me to pick up the phone and to call the people. I am grateful to you for giving a lot of your time to answer my questions and doubts.

I want to thank Adèle, 3rd year PHD-student on the ForCa-G experiment, who answered my too many stupid questions which I did not dare to ask Franck. Thank you also for your numerous comments on this manuscript and for your commitment to the "PHD-Student-Union" whithout which there would not be such a joyful atmosphere among the students.

I want to thank Min-Kang, post-doctoral researcher on the ForCa-G experiment, who helped me to relax when I broke the crystal. Thank you also for your great patience during our teamwork on the Verdi laser, I wish you the best for your new position in Wuhan.

I want to thank Peter for the two interesting discussions we had in Stockholm and in Paris about frequency doubling and amplifiers. I wish you the best for your PHD. I thank Bruno, former PHD-student on the experiment, for giving me this LaTeX template. I thank the workshop-team for helping me designing the mounting system for the oven. I thank Peter Wolf for lending me the 50W amplifier. I thank the whole "Capteurs Inertiels" team whose every members contribute to the wonderful working atmosphere in **SYRTE**.

Finally I want to thank you Fredrik for showing your interest in my work by accepting to be my examiner. Thank you for your help and your several answers to my questions. It was a pleasure to discuss the physics with you as well as the Swedish-French disparities !

References

[1] Q. Beaufils, G. Tackmann, X. Wang, B. Pelle, S. Pélisson, P. Wolf, and F. Pereira dos Santos. "Laser controlled tunneling in a vertical optical lattice". *Phys. Rev. Lett.*, 106(21):213002, May 2011.

[2] F. Bloch. Über die Quantenmechanik der Elektronen in Kristallgittern. *Zeitschrift für Physik*, 52:555–600, July 1929.

[3] G. D. Boyd and D. A. Kleinman. "Parametric Interaction of Focused Gaussian Light Beams". *J. Appl. Phys.*, 39:3597, Jul 1968.

[4] A. Bruner, B. Eger, M. B. Oron, P. Blau, and M. Katz. "Temperature-dependent Sellmeier equation for the refractive index of stoichiometric lithium tantalate". *Opt. Lett.*, 28:194, Feb 2003.

[5] O. Carnal and J. Mlynek. "Young's double-slit experiment with atoms: A simple atom interferometer". *Phys. Rev. Lett.*, 66(21):2689–2692, May 1991.

[6] S. Chaitanya Kumar, G. K. Samanta, and M. Ebrahim-Zadeh. "High-power, single-frequency, continuous-wave second-harmonic-generation of ytterbium fiber laser in PPKTP and MgO:sPPLT". *Opt. Express*, 17:13711, Aug 2009.

[7] R. Charrière, M. Cadoret, N. Zahzam, Y. Bidel, and A. Bresson. "Local gravity measurement with the combination of atom interferometry and Bloch oscillations". *Phys. Rev. A*, 85:013639, Jan 2012.

[8] C. Davisson and H. Germer. "The scattering of electrons by a single crystal of nickel". *Nature*, 119:558–560, 1927.

[9] M. M. Fejer, G. A. Magel, D. H. Jundt, and R. L. Byer. "Quasi-Phase-Matched Second Harmonic Generation: Tuning and Tolerances". *IEEE Journal of Quantum Electronics*, 28:2631, Nov 1992.

[10] Z.-K. Hu, B.-L. Sun, X.-C Duan, M.-K. Zhou, L.-L Chen, S. Zhan, Zhang K.-Z, and J. Luo. "Demonstration of an ultrahigh-sensitivity atom-interferometry absolute gravimeter". *Phys. Rev. A*, 88:043610, Oct 2013.

[11] B. Pelle. *Interféromètres atomiques dans un réseau optique.* PhD thesis, Université Pierre et Marie Curie (Paris 6), 2013.

[12] B. Pelle, A. Hilico, G. Tackmann, Q. Beaufils, and F. Pereira dos Santos. "State-labeling Wannier-Stark atomic interferometers". *Phys. Rev. A*, 87(2):023601, Feb 2013.

[13] G. Tackmann, B. Pelle, A. Hilico, Q. Beaufils, and F. Pereira dos Santos. "Raman-laser spectroscopy of Wannier-Stark states". *Phys. Rev. A*, 84(6):063422, Dec 2011.

[14] M. Takamoto, F.-L. Hong, R. Higashi, and H. Katori. "An optical lattice clock". *Nature*, 435(7040):321–324, 2005.

[15] P. Wolf, P. Lemonde, A. Lambrecht, S. Bize, A. Landragin, and A. Clairon. "From optical lattice clocks to the measurement of forces in the Casimir regime". *Phys. Rev. A*, 75:063608, Jun 2007.

[16] M.-K. Zhou, B. Pelle, A. Hilico, and F. Pereira dos Santos. "Atomic multiwave interferometer in an optical lattice". *Phys. Rev. A*, 88:013604, Jul 2013.